UC Merced

UC Merced Electronic Theses and Dissertations

Title

Optical properties of hybrid perovskite thin films and quantum dots for solar device applications

Permalink

https://escholarship.org/uc/item/0k5177cs

Author

Colabewala, Benaz

Publication Date

2020

Peer reviewed|Thesis/dissertation

eScholarship.org Powered by the California Digital Library
University of California

Optical properties of hybrid perovskite thin films and quantum dots for solar device applications

by

Benaz Colabewala

A dissertation submitted in partial satisfaction of the
requirements for the degree of
Doctor of Philosophy

in

Physics

in the

GRADUATE DIVISION
of the
UNIVERSITY OF CALIFORNIA, MERCED

Committee in charge:
Professor Jay E. Sharping, Chair
Professor Boaz Ilan
Professor Sayantani Ghosh, Advisor

2020

Optical properties of hybrid perovskite thin films and quantum dots for solar device applications

© 2020 Benaz Colabewala

The dissertation of Benaz Colabewala is approved:

Chair Date

Date

Advisor Date

University of California, Merced

2020

To my parents, who taught me the meaning of
dedication, sacrifice and kindness. And to my brother, who
taught me to not take things too seriously.

Acknowledgments

I wish to acknowledge all the people without whom the completion of this work would not have been possible. I would like to thank my committee and especially my advisor, Sayantani Ghosh, for their mentorship and guidance throughout my graduate experience. Thank you Sai for the wisdom, compassion and patience that allowed me to overcome my failures and persevere towards my goals. I am grateful to my lab mates for all of their assistance and friendship. I wish to thank Som Sarang and Katerina Nikolaidou for their help in preparation of perovskite thin films, Will Delmas and Albert DiBenidetto for their contributions to my work with perovskite quantum dots, and Mark Bartolo for his assistance with spatially resolved photoluminescence spectroscopy. I would also like to thank Professor Boaz Ilan and his student Christine Hoffman for their collaboration in providing insightful simulations for my luminescent solar concentrator project. Finally, I am grateful for the unwavering support of my family and friends without whom this endeavor would never have been completed. I want to thank my mom, dad, my brother Eric, and all of my southern California friends for always making me feel loved and supported despite the miles between us. And thank you Al, Katie and Daniel for all your kindness in Merced. You were my family away from home and made the hardest times easier.

I wish to acknowledge the funding support that allowed me to complete much of this work, which includes the Graduate Dean's Dissertation Fellowship, Physics Summer Fellowship and Dan David Solar Fellowship. I am grateful for the freedom this financial support gave me to focus on my research.

A portion of the text of this dissertation is a reprint of the material as it appears in "The potential of scalability in high efficiency hybrid perovskite thin film luminescent solar concentrators." (Solar Energy, Volume 183, 2019). The input of my co-authors was instrumental in the development of this work.

Curriculum vitae

Academic Background

Ph.D.	Physics, University of California, Merced August 2014 - Current
B.Sc	Physics, California State University, Long Beach August 2008 - May 2012

Publications

- Mendewala B., Nikolaidou K., Hoffman C., Sarang S., Lu J., Ilan B., Ghosh S. (2019). The potential of scalability in high efficiency hybrid perovskite thin film luminescent solar concentrators. *Solar Energy, 183*, 392-397.
- Nikolaidou K., Sarang S., Hoffman C., Mendewala B., Ishihara H., Lu J.Q., Ilan B., Tung V., Ghosh S. (2016). Hybrid perovskite thin films as highly efficient luminescent solar concentrators. *Applied Optical Materials, 4*(12), 2126-2132.
- Colabewala B., Jiang L., Winston R. (2015). String method of nonimaging optics from a radiation theory perspective. *Proc. SPIE 9572, Nonimaging Optics: Efficient Design for Illumination and Solar Concentration XII* 957202.

Oral Presentations

- *Hybrid Perovskite Thin Films as Highly Efficient Luminescent Solar Concentrators*, Optics and Lasers 2019; San Francisco, California. (June 2019)
- *Exploring resonant interaction between hybrid lead-halide perovskite quantum dots and plasmonic metal nanoparticles*, APS March Meeting 2018; Los Angeles, California. (March 2018)
- *Scalability and optimization of hybrid perovskite thin films as luminescent solar concentrators*, APS Far West Section 2017; Merced, California. (October 2017)
- *Optimization of hybrid perovskite thin films as luminescent solar concentrators*, APS March Meeting 2017; New Orleans, Louisiana. (March 2017)
- *String method of nonimagingoptics from a radiation theory perspective*, SPIE 9572; San Diego, California. (August 2015)

Academic Awards

June 2020	Graduate Dean's Dissertation Fellowship
October 2017	Margaret Burbidge Award for Best Experimental Research
June 2017	Physics Summer Research Fellowship

September 2015	Dan David Solar Fellowship
2015, 2016	Physics Research Travel Award

Teaching Experience

Introductory Physics (Mechanics)	*Fall 2014, Spring 2015, Fall 2015, Spring 2016, Fall 2019, Spring 2020*
Introductory Physics (Electromagnetism)	*Summer 2015, Summer 2016, Fall 2016, Spring 2017, Spring 2018*
Introductory Calculus	*Fall 2017, Spring 2019, Summer 2019*

Abstract

Optical properties of hybrid perovskite thin films and quantum dots for solar device applications

by

Benaz Colabewala
Doctor of Philosophy in Physics

University of California, Merced

Professor Jay E. Sharping, Chair

Hybrid perovskite materials are an emergent class of materials that display optical and electronic qualities highly favorable to solar device applications. Their affordability combined with high efficiencies have propelled them to the forefront of modern solar energy research. This dissertation investigates the unique optical properties of perovskite thin films and perovskite-based quantum dots using a variety of spectroscopy methods to demonstrate their potential for a variety of solar device applications, particularly luminescent solar concentrators (LSCs).

LSCs are a low-cost, design-friendly alternative to traditional solar cells that typically consist of a fluorescent material atop a high refractive index that absorbs incident light and re-emits it at a lower energy, acting as a waveguide for the down-shifted sunlight to its edges, where a solar cell is attached. Perovskites make excellent candidates for LSCs due to their high quantum yield, large refractive index and large Stokes shift. We optimize the halide content and thickness of perovskite thin films to yield devices reaching a maximum optical efficiency of 34.7% for 1.5cm x 1.5cm samples.

Additionally, we investigate the effects of coupling between perovskite quantum dots and plasmonic gold nanoparticles to illuminate the nature of this interaction. The collective resonance of free electrons in metallic nanoparticles can couple with the electron-hole pair in an excited semiconductor and lead to a number of fascinating phenomena. We perform photoluminescence and lifetime measurements on perovskite quantum dots in contact with gold nanoparticles of varying sizes, which result in emission enhancement for smaller nanoparticles.

These results then encourage us to explore the viability of the perovskite quantum dot/gold nanoparticle system as a highly efficient LSC. Through dip-coating and optimizing gold nanoparticle concentration, we produce large-scale, uniform, competitively efficient LSCs reaching a maximum efficiency of 2.87% for 10cm x 10cm samples.

Contents

List of Figures

Chapter 1

Motivation and Introduction

Human energy consumption is currently increasing at an unsustainable rate.[1] The rising temperature of the Earth's atmosphere, increasing costs of coal and crude oil, and the rapid destruction of our planet's natural resources all demand an alternative, renewable energy solution. Researchers have found promising candidates in solar harnessing devices, where solar cells with 20% efficiency covering less than 1% of the Earth's surface area can meet the entire planet's projected energy demand in 2030.[2] However, such large-scale implementation is still unattainable due to high initial costs and lack of supporting infrastructure. As a result, current research in solar energy is focused on optimization of these devices to be lower in cost and higher in efficiency.[1, 3]

While the most common commercial photovoltaics (PVs) are made with single crystalline silicon, the high manufacturing costs remain a major obstacle to widespread implementation.[3] While cheaper alternatives such as dye-sensitized solar cells have been extensively studied, their low efficiency bars them from being an attractive alternative.[4] On the other hand, gallium arsenide triple-junction cells have shown remarkably high efficiency in lab, but remain prohibitively expensive for any kind of large-scale manufacturing.[5] Since most PV technologies follow this general trend of trading off efficiency for affordability, the emergence of perovskite-based photovoltaics (PPVs) has been a breakthrough where the low-cost, easily processed material has been shown to have impressive efficiency of 25.2% comparable to commercial silicon, as shown in Fig. 1.1.[6, 7] However, PPVs still face significant challenges in stability and toxicity, and further improvements to efficiency are still needed before commercialization can become a possibility.

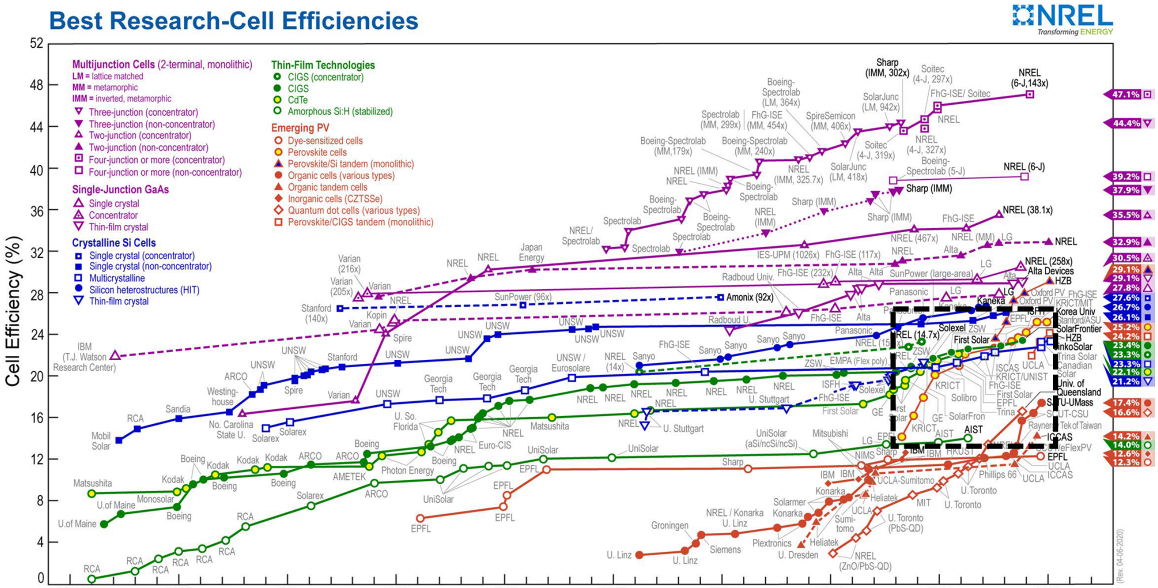

Figure 1.1: Commercial solar cell efficiencies as of 2020. PPV is outlined. This plot is courtesy of the National Renewable Energy Laboratory, Golden, CO.

This dissertation aims to address some of these challenges through the investigation and improvement of optical properties of hybrid perovskite (PVSK) materials, including perovskite thin films and perovskite-based quantum dots (PQDs). Chapter 2 reviews the scientific background for the materials, devices and physical concepts discussed throughout this work, while Chapter 3 details the experimental methods utilized in each project. Chapters 4 through 6 describe the projects completed and the results obtained, and Chapter 7 provides a summary and outlook on future progress in the field.

The first project studies PVSK thin films in the context of luminescent solar concentrators (LSCs). Planar LSCs generally consist of a fluorescent material atop a high refractive index substrate that absorbs incident light and re-emits it at a lower energy, acting as a waveguide for the down-converted sunlight to its edges where a solar cell is attached. The down-conversion ensures that light will not be re-absorbed by the LSC material, and its efficiency can be further increased by spectrally matching the LSC's emission to the absorption of the solar cell. LSCs are low-cost alternatives to traditional PV systems whose benefits include being lightweight and able to operate under both diffuse and direct sunlight. Due to their superior optical properties such as high quantum yield, broad absorption spectra and high refractive index, PVSK thin films were proven to be viable candidates for the active medium in LSCs in our previous work. In this project, we investigate the roles of halide composition, morphology and film thickness in PVSK LSCs to optimize optical efficiency.

The second project focuses on improving optical emission of PVSK thin films and PQDs via plasmonic gold nanoparticles (AuNPs). The field of nanoplasmonics is rapidly advancing due to its many applications in PV, displays and sensing. When excited at their resonance frequency, metallic nanoparticles can generate localized electric fields that can enhance optical properties of, or transfer energy to, surrounding media. The coupling between plasmonic nanoparticles and quantum dot (QD) excitons has been well documented, displaying favorable characteristics such as reduced lifetime and suppressed blinking. Furthermore, plasmonic nanoparticles have been previously utilized in thin film devices to improve optical characteristics. While traditional CdSe QDs have most commonly been used for these studies, the interaction between PQDs and plasmonic nanoparticles has been largely uninvestigated. PQDs have distinct advantages over conventional QDs, including high quantum yield and ease of compositional tunability. For this project, we study the nature of the plasmon-exciton coupling and its effect on PQD and PVSK thin film optical properties.

The final project revisits PVSK LSCs and aims to implement the results of the previous two projects into the design of a large-scale, high efficiency LSC utilizing PQDs coupled with AuNPs. LSCs made with QDs have been extensively studied and found to be successful due to their broad absorption across visible spectra, so it follows that PQDs would naturally be viable candidates for high efficiency LSCs due to their superior optical properties over conventional QDs. By implementing AuNPs into our LSC devices, we can further increase the emission and optical efficiency. Since QD LSCs also benefit from low reabsorption due to the discrete nature of QDs, we investigate scalability by producing large-scale devices to maximize both optical efficiency and geometric gain.

Chapter 2

Background

2.1 Hybrid perovskite materials

2.1.1 Crystal structure

Hybrid inorganic-organic perovskites are direct band gap semiconductors that typically form the structure ABX_3, B is a metal cation and C is a halide ion, as shown in Fig. 2.1(a). [8, 9] The large organic cation is often methylammonium (MA), but more recently formamidinium (FA) has also been used and occasionally cesium will be utilized to make a fully-inorganic structure. It has been shown that the band gap is very sensitive to the size of the large cation, with larger sizes leading to reduced band gaps. While the Cs cation improves stability, this comes at the cost of an increase in band gap since it is smaller than both MA and FA. [10] The metal cation is often lead, but tin has occasionally been used as well, and the halide ion varies depending on the desired structural or organic properties. At room temperature, PVSKs form the tetrahedral structure shown in Fig. 2.1(a). Hybrid PVSKs allow for the low cost solution-processing of organic materials while demonstrating the high carrier mobility and lifetime of inorganic materials. Additionally, by varying A, B or X, the bandgap can be tuned as shown in Fig. 2.1(b).

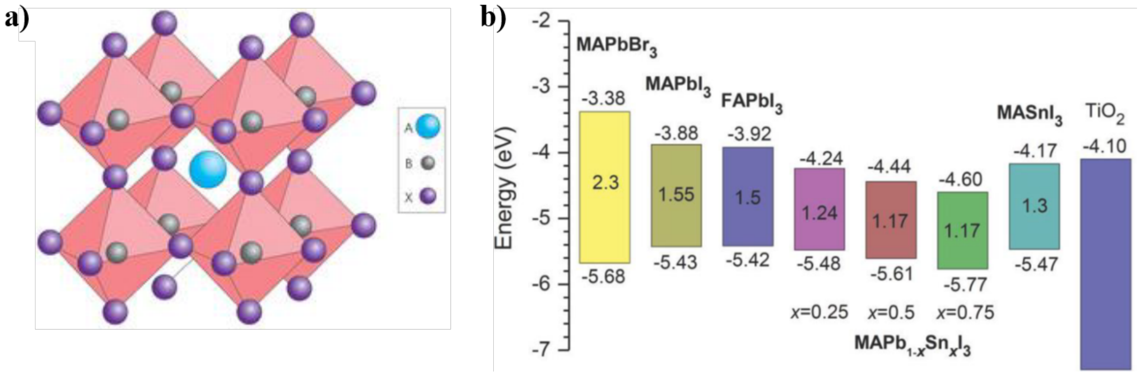

Figure 2.1: (a) Crystal structure of room temperature perovskite and (b) Energy bands for varying compositions of PVSK. Reprinted with permission from Nature Photonics. [9]

2.1.2 Optical properties

Perovskite semiconductors have one of the highest absorption coefficients among conventional photovoltaic materials, measured around 10^5/cm. This is partly due to the previously mentioned direct band gap, which does not require phonon contributions to transition from the optical to valence band, as well as a high density of states in both the valence and conduction band. PVSK semiconductors are ionic in nature, where the conduction band generally contains the Pb-p states, while the valence band containes the Pb-s states and the p states of the chosen halide. This pair of Pb-s electrons in the valence band near the maximum contributes to the high density of states and resulting high absorption coefficient.

PVSKs have a broad absorption spectrum that make them well-suited to PV technologies, as well as high quantum yield (QY) reported at nearly 80%. [9] However, charge transport in PVSKs suffers from the presence of trap states, particularly at grain boundaries. These charge transport properties are widely tunable by varying the lead halide, which later chapters will show affects the thin film optical properties as well. Specifically, $MAPbI_3$ made with lead acetate demonstrates a reduced concentration of iodide which results in a lower defect density and prevents the formation of deep traps, despite forming smaller grains (and thus more grain boundaries). This results in longer charge diffusion lengths of 600 nm compared to 100 nm for iodide-only samples, which is desirable in PVs. [11]

2.1.3 Spin and Magnetic properties

Perovskites additionally display interesting spin and magnetic properties due to their unique molecular structure. Since the large organic cation is not symmetrically centered in the molecule, its dipole moment can cause the molecule to become spontaneously electrically polarized from a lack of inversion symmetry, resulting in ferroelectric regions that allow for ideal photovoltaic properties, such as voltages higher than the band gap along with large charge carrier separation. [12] This cation polarization additionally results in lattice polarization, which can further contribute to the rise of ferroelectric behavior. [13]

The lack of inversion symmetry also allows for spin-orbit coupling, which results in energy band splitting, known as the Rashba effect. In perovskites, this coupling theoretically arises in a splitting of the conduction band from the spin degeneracy, which creates spin-allowed and spin-forbidden recombination channels. [14] As the spin and momentum are non-degenerate in the spin-forbidden path, the recombination rate would be much slower. By slowing the recombination rate of the spin-allowed path through fast recombination at the band edges, this coupling is one possible explanation of the long carrier diffusion lifetimes present in halide perovskites. [14] However, convincing experimental evidence of this coupling remains to be found. Further investigation into the unique spin and magnetic properties of perovskite could provide rich and interesting new semiconductor physics for a variety of applications beyond solar.

2.1.4 Perovskite quantum dots

Quantum dots are semiconducting nanoparticles in which quantum confinement occurs as a result of one dimension being near to or smaller than its exciton Bohr radius. [15] Recently, perovskite quantum dots have emerged as a new interesting class of nanocrystals with attractive optical properties such as high photoluminescence quantum yield (up to 90%) and widely tunable emission wavelength by varying lead halide content. [16] Figure 2.2 shows the tunability of peak emission in $CsPbI_xBr_{3-x}$ PQDs from 400-800 nm by varying the I:Br ratio. [17] Additionally, the high temperature stability and narrow band emission (20 nm) due to an increase in bound states relative to the bulk material makes PQDs ideal candidates for laser and LED display applications. The ease of fabrication of colloidal QDs also make them attractive for PV applications. [15] For our research, PQDs present an opportunity to understand fundamental processes without the heterogeneity present in bulk PVSK thin films, which can be valuable to future PVSK and other QD PV research.

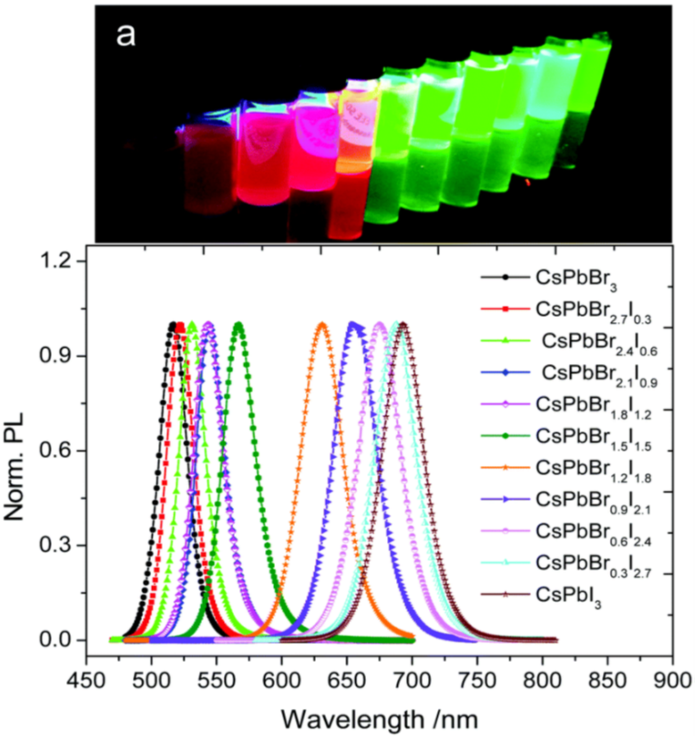

Figure 2.2: Peak emission shift of $CsPbI_xBr_{3-x}$ as halide content is varied. Reprinted with permission from Nanoscale. [17]

2.2 Perovskite photovoltaics

2.2.1 Thin films

Perovskite-based photovoltaics have the benefit of being simultaneously low-cost and high-efficiency, with the power conversion efficiency (PCE) improving more rapidly over time than any other standard reported PV technology. PPVs were first introduced in 2009, where MAPbI3 was used as the active material and reported PCE of 3.81%. [18] Only seven years later in 2016, researchers had improved PCE to 22.1%. [7] Device engineering has focused on improving PCE through fabricating more uniform films and more efficient electron- or hole-transport layers, as well as improving stability. PVSK stability remains the largest obstacle thus far, where inorganic-only PPVs have been fabricated to remain stable over several months, at the cost of reduced efficiency. [9]

2.2.2 Quantum dots

Photovoltaics employing QDs as a light-harvesting medium have gained popularity due to their ability to improve range of absorption in tandem cells and improve charge carrier generation through multiple exciton generation (MEG). [15] Due to the ease of bandgap tunability, QDs can be strategically chosen to maximize absorption range in a tandem PV cell. [15] Additionally, MEG has been observed in QDs where a single photon generates multiple low-energy electron-hole pairs rather than a single high-energy exciton pair, which in turn increases the overall photocurrent of the device. [19] A blend of polymer and CdSe QDs for example have demonstrated increased charge separation and photocurrent enhancement under visible light. [15] Despite these attractive properties, QDs face significant challenges in stability and toxicity, while QD PVs remain low-efficiency on their own due to high recombination rates of charge carriers. [15]

2.3 Luminescent solar concentrators

2.3.1 Device Physics

Luminescent solar concentrators (LSCs) typically consist of a fluorescent material on top of a high refractive index substrate that absorbs incident light and acts as a waveguide for it to be re-emitted it at its edge where a solar cell is attached. [20] The emitted light is downconverted to a lower energy which prevents it from being reabsorbed by the LSC material. Advantages of LSCs include being lightweight, low-cost and able to operate under both diffuse and direct sunlight. [21] A simple schematic of an LSC is shown in Fig. 2.3. The main metric used to qualify LSCs is optical efficiency η_{opt}, which is defined as:

$$\eta_{opt} = \frac{I_{\text{LSC}} \cdot A_{\text{PV}}}{A_{\text{LSC}} \cdot I_{\text{PV}}} \tag{2.1}$$

where I_{LSC} and I_{PV} are the current generated by the PV with and without the attached LSC respectively, and A_{LSC} and A_{PV} are the areas of the LSC and PV.

There are a number of mechanisms which inhibit η_{opt} and have prevented LSCs from becoming commercially viable thus far. A diagram illustrating these loss mechanisms is shown in Fig. 2.4. [22] The first loss mechanism (Fig. 2.4.1) occurs when incident light is absorbed by the luminophore and re-emitted at an angle outside of the "capture" cone of the waveguide, and thus is not internally reflected but exits out the surface of the LSC. These surface losses can be mitigated by employing selective mirrors and aligning the luminophores. [23, 24]

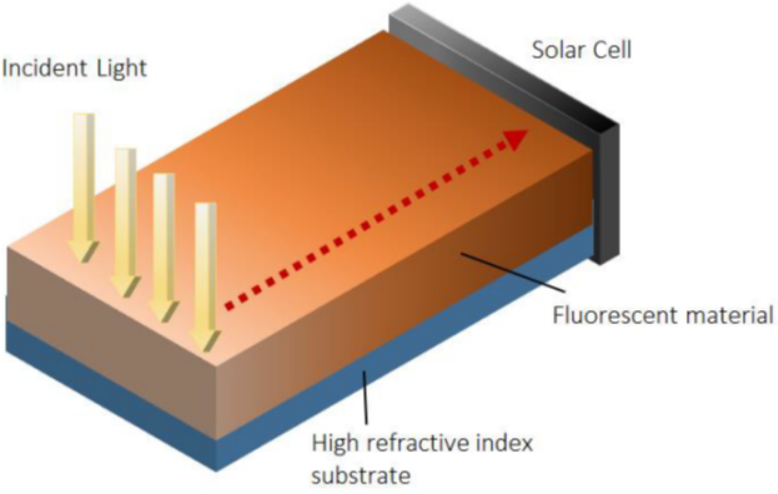

Figure 2.3: Schematic of planar LSC. Incident light is absorbed by the luminophore and downconverted to a lower energy. The downshifted light is internally reflected and absorbed by a solar cell attached to the edge of the concentrator.

The second type of loss in an LSC (Fig. 2.4.2) occurs when the emission from the luminophore is re-absorbed by another luminescent molecule further down the waveguide, preventing the emission from reaching the attached solar cell. This self absorption is mainly due to spectral overlap between the material's absorption and emission bands, quantifed by the overlap factor f_a that is defined as the ratio of overlap between the absorption and emission spectra to the emission spectra. [25] Self-absorption losses can be mitigated in a number of ways, including selecting materials with larger Stokes shifts that limit this overlap naturally, utilizing thinner layers to limit re-absorption events and doping active layers to increase separation between the absorption and emission bands of the material.

The third illustrated loss mechanism (Fig. 2.4.3) is of losses directly caused by the inherent material properties of the luminophore selected, such as the location of its optical bands and stability. When the wavelength of incident light is outside the material's absorption spectra, it will pass through the LSC without being absorbed at all as in Fig. 2.4.3a. When high energy photons are absorbed that result in photodegradation of the luminophore species, the LSC will suffer from lower overall emission, as shown in Fig. 2.4.3b. Additionally, the fluorescence quantum yield of a material will limit the re-emission of every absorbed photon, as the energy will be transferred to heat or phonon vibrations instead, as shown in Fig. 2.4.3c. These losses are generally only mitigated through thoughtful selection of the active LSC material. A more thorough discussion of the most common luminophores and their advantages and drawbacks is provided in the next section.

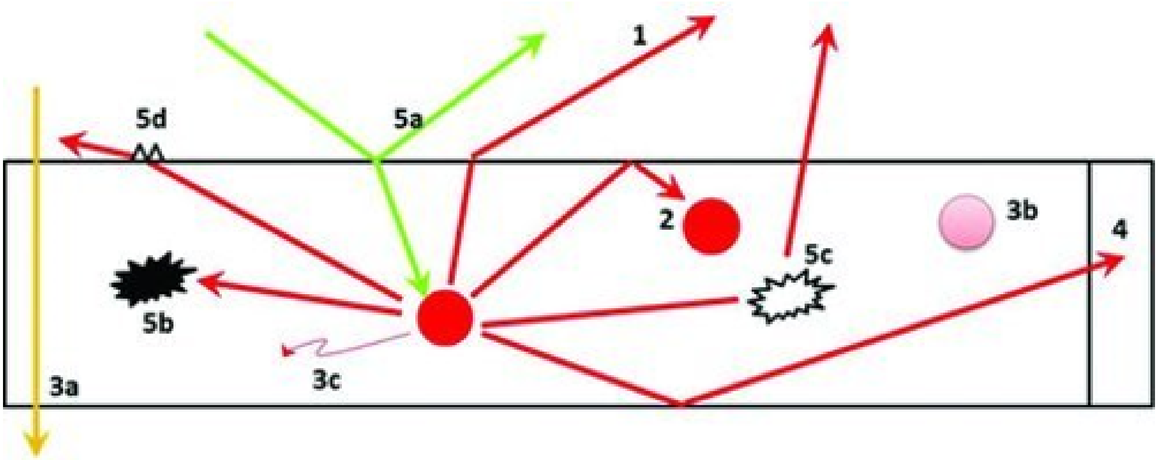

Figure 2.4: Loss mechanisms in luminescent solar concentrators: 1) Light emitted outside capture cone; 2) re-absorption of emitted light by another luminophore; 3a) input light is not absorbed by the luminophore; 3b) limited luminophore stability; 3c) internal quantum efficiency of the luminophore is not unity; 4) solar cell losses; 5a) reflection from the waveguide surface; 5b) absorption of emitted light by the waveguide; 5c) internal waveguide scattering; 5d) surface scattering. Reprinted with permission from Wiley [Copyright ©2012 WILEY-VCH Verlag GmbH Co. KGaA, Weinheim].

Finally, some of the loss mechanisms in a complete LSC-PV system arise not from the concentrator material itself, but from the attached solar cell device and waveguide. Fresnel reflection will cause a fraction of the incident light to reflect off the surface of the concentrator without ever being absorbed (Fig. 2.4.5a). Then, small imperfections in the waveguide can cause absorption of the LSC emission by the waveguide or internal or surface scattering, as shown in Fig. 2.4.5b-d. Finally, even if the emitted light avoids all these other loss mechanisms and reaches the attached PV cell, ths solar cell itself has a limited conversion efficiency and thus cannot absorb every photon incident from the concentrator (Fig. 2.4.4).

While engineering LSC-PV devices that limit surface, waveguide or PV-related losses is a rich topic for research, mitigating these losses is beyond the scope of this work. The following chapters focus on optimizing optical properties of carefully selected materials that limit self-absorption and maximize emission from the LSC active layer to optimize optical efficiency.

2.3.2 Material Selection

When LSCs were first introduced in the 1970s, research focused on employing organic fluorescent dyes due to their affordability, ease of manufacturing and high absorption coefficients. [22] While an extensive variety of dyes have been studied for LSCs over the years, the most popular dye types have been rhodamines, coumarins, and perylene dyes. [26, 25, 27] Earliest research focused primarily on rhodamines and coumarines while perylene dyes gained more attention about a decade after LSC research began. Rhodamine dyes are desirable due to their high solubility and high quantum yields, but have a low Stokes shift and thus lead to high re-absorption. [28] Coumarins have a much higher Stokes shift than rhodamines; for example, f_a for Coumarin 540A is 0.12 whereas it is 0.48 for Rhodamine 6G. [29] However, coumarins exhibit generally poor photostability which limits their use as LSCs. Perylene and perylene derivatives exhibit both high quantum effieciency and better photostability, but suffer from poor solubility. [30] An extensive amount of research has been done to optimize each of these properties in dye-based LSCs, but organic dyes in general suffer from a limited absorption spectra and photodegradation. [30]

In the early 2000s, quantum dots were introduced as an alternative to dye-based concentrators due to their higher photostability, large Stokes shift, tunable optical properties and wide absorption spectra. [31] The most commonly used quantum dots for LSCs were CdSe/ZnS and PbS, as these were also popular materials for QD-based solar cells for the same desirable optical properties. [32] While cadmium-based LSCs were easy to fabricate and tune, PbS QDs had overall higher absorption efficiencies that made them attractive LSC candidates as well. [33] However, quantum dots in general suffered from lower overall quantum yield and high toxicity.

As with photovoltaics, every luminophore proposed for active LSC layers has distinct advantages and disadvantages, and so there is no widely agreed upon "ideal" LSC material in literature. In this work, we study perovskite thin films and quantum dots as active absorbers in LSCs due to their unique optical properties that align with many of the requirements for optimal LSC materials.

2.4 Plasmonic nanoparticles

2.4.1 Localized surface plasmon resonance

Plasmonic nanoparticles are characterized by charge density oscillation of conduction band electrons upon photoexcitation, otherwise known as localized surface plasmon resonance (LSPR). This resonance occurs when the incident light frequency ω matches the surface plasmon resonance frequency ω_{sp} of the metallic nanoparticle which is given by [34]

$$\omega_{sp} = \frac{\omega_P}{\sqrt{1+2\epsilon}}\sqrt{1+(1+2\epsilon_m)\left(\frac{R_0}{R}\right)^2} \tag{2.2}$$

where ϵ_m is the dielectric constant of the surrounding medium, R is the radius of the nanoparticle and ω_P is the bulk plasma frequency given by

$$\omega_P = \sqrt{\frac{4\pi n_e e^2}{m_e}} \tag{2.3}$$

and R_0 is

$$R_0 = \sqrt{\frac{3\pi\hbar^2}{4m_e^2 k_F}} \tag{2.4}$$

where k_F is the Fermi wave vector, and e and m_e are the charge and mass of an electron respectively. [35] Incident light on a nanoparticle can be effectively modeled as a metallic sphere in a uniform external field, where a polarization vector will be generated in the direction of the field and thus a dipole field will be induced in the nanoparticle in the opposite direction of the incident light, which will result in the light extinction. [35] Assuming homogeneous, spherical nanoparticles, Mie theory provides the total extinction Q_{ext} and scattering efficiency Q_{sca} as an infinite series:

$$Q_{ext} = \frac{2}{x^2}\sum_{n=1}^{\infty}(2n+1)\mathrm{Re}[a_n + b_n] \tag{2.5}$$

$$Q_{sca} = \frac{2}{x^2}\sum_{n=1}^{\infty}(2n+1)[a_n^2 + b_n^2] \tag{2.6}$$

where

$$a_n = \frac{m\psi_n(mx)\psi_n'(x) - \psi_n(x)y_n'(mx)}{m\psi_n(mx)\xi_n'(x) - m\xi_n(x)\psi_n'(mx)} \tag{2.7}$$

$$b_n = \frac{\psi_n(mx)\psi_n'(x) - m\psi_n(x)y_n'(mx)}{\psi_n(mx)\xi_n'(x) - m\xi_n(x)\psi_n'(mx)} \tag{2.8}$$

where n is the refractive index of the sphere, m is the ratio of n to the refractive index of the surrounding medium n_m, x is the size parameter given as $2\pi n_m R/\lambda$ (R is nanoparticle radius and λ is the wavelength of incident light), ψ_n and ξ_n are the Riccati-Bessel functions, and the prime indicates first differentiation with respect to the argument in parentheses. The absorption efficiency Q_{abs} is then given by

$$Q_{abs} = Q_{ext} - Q_{sca} \tag{2.9}$$

since all light that is not scattered will be absorbed. [35] Thus, by varying the size, geometry and surrounding medium, the absorption and scattering ratio can be controlled. Figure 2.5 shows the percent of light scattered and absorbed calculated as a function of diameter for a gold nanosphere integrated from 300—800 nm.

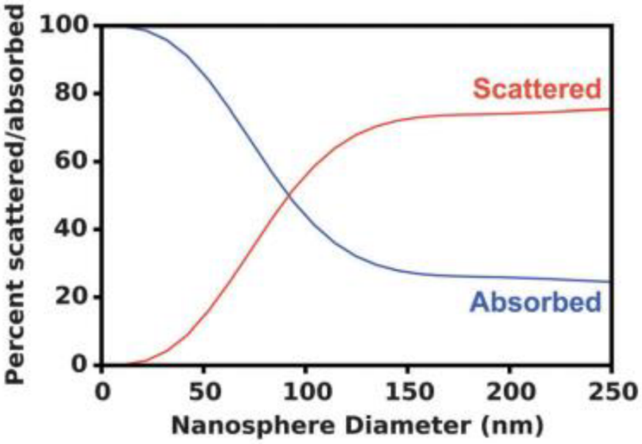

Figure 2.5: Percent of light scattered and absorbed calculated as a function of Au nanosphere diameter integrated from 300-800 nm. Republished with permission from the Royal Society of Chemistry. [36]

2.4.2 Plasmon-semiconductor interactions

Near-field Enhancement

Near-field enhancement occurs when LSPR leads to local enhancement of electromagnetic fields in the immediate vicinity (< 50 nm away) of nanostructures. This allows the nanoparticles to act as secondary light sources that increase the overall light absorbed by the PV. These enhanced fields are generally orders of magnitude higher in intensity than the incident light, but also fall off very rapidly as distance increases. [37] Figure 2.6 shows the calculated near-field enhancement as a function of distance from the nanoparticle surface for gold and silver nanospheres and nanocubes. [36] From this, it is clear that in order to benefit from near-field enhancement, the semiconductor molecules must be very close to the nanoparticles in the PV.

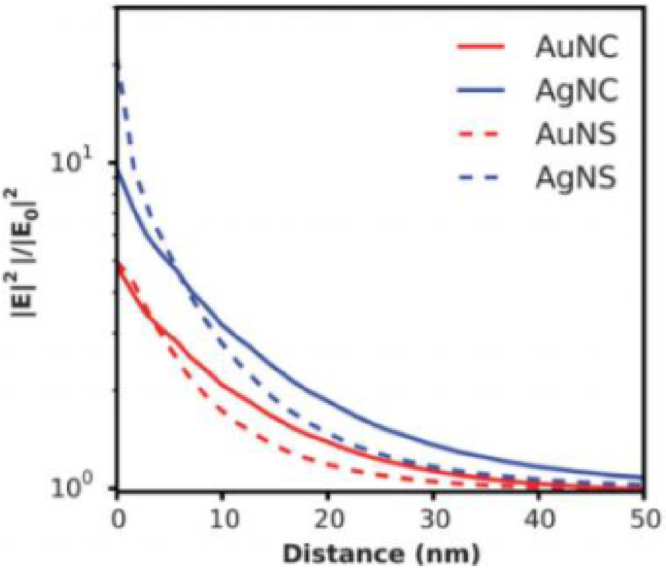

Figure 2.6: Calculated near field enhancement as a function of distance from the particle surface averaged over the 300–800 nm spectral range for Au and Ag nanospheres and cubes.

Due to the very small range of this effect, it will be experimentally difficult to probe near-field enhancement directly. However, for particles too small to provide far-field scattering, enhanced absorption could indicate near-field enhancement by process of elimination. As with far-field scattering, the composition, size and shape of the nanoparticle will affect the range and intensity of enhancement.

Hot Electron Transfer

When a plasmon decays non-radiatively on a femtosecond timescale, the energetic reaction creates electron-hole pairs with a higher thermal energy than the metallic atoms. These hot electrons eventually cool down through electron-electron scattering and electron-phonon collisions. [38] Because of their high energy, these hot electrons can transfer to the conduction band of a surrounding semiconductor, thus leading to charge carrier enhancement in the PV cell. As shown in Figure 2.7, this will occur only if the Fermi levels of the plasmon and the semiconductor match. Additionally, in most plasmon-enhanced PV systems, the metallic nanoparticles are coated by an insulating interlayer such as SiO2 to minimize damping. In order for hot electron transfer to occur, there must also be minimal separation (< 3 nm) between the semiconductor and nanoparticle by any insulating layer coating the nanoparticles. [39]

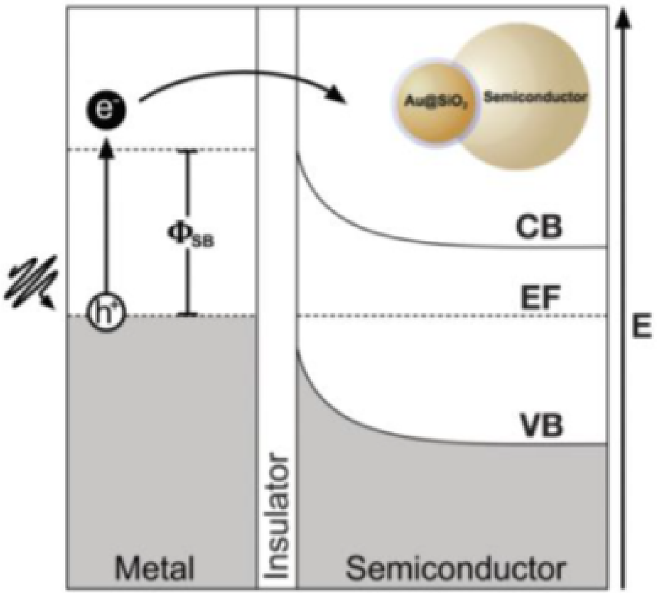

Figure 2.7: Schematic energy diagram of hot-electron transfer process: first, plasmon decoherence produces hot electron-hole pairs and next, hot electrons with sufficiently high energy travel through the Schottky barrier and a thin insulator to enter the conduction band of the semiconductor material.

Hot-electron transfer can be characterized by observation of enhanced charge carrier generation using photocurrent measurements compared to a control. It has been demonstrated that while larger nanoparticles will produce more hot electrons with lower energy, smaller nanoparticles will produce less hot electrons with higher energy. [40] Nanostructures $<$ 20 nm in size have been observed to be most efficient at generating hot electrons in semiconductors. [41]

Plasmon Resonant Energy Transfer

Plasmon resonant energy transfer (PRET) occurs when resonant energy is transferred from the metallic nanoparticle to the semiconductor molecule via dipole-dipole coupling, thereby generating electron-hole pairs in the semiconductor near the band edge. [42] This mechanism is illustrated in Figure 2.8. While band alignment is not necessary for PRET as in hot electron transfer, a spectral overlap in absorption is needed between the semiconductor and nanoparticle. Additionally, there is no constraint on the insulating layer for PRET. [43]

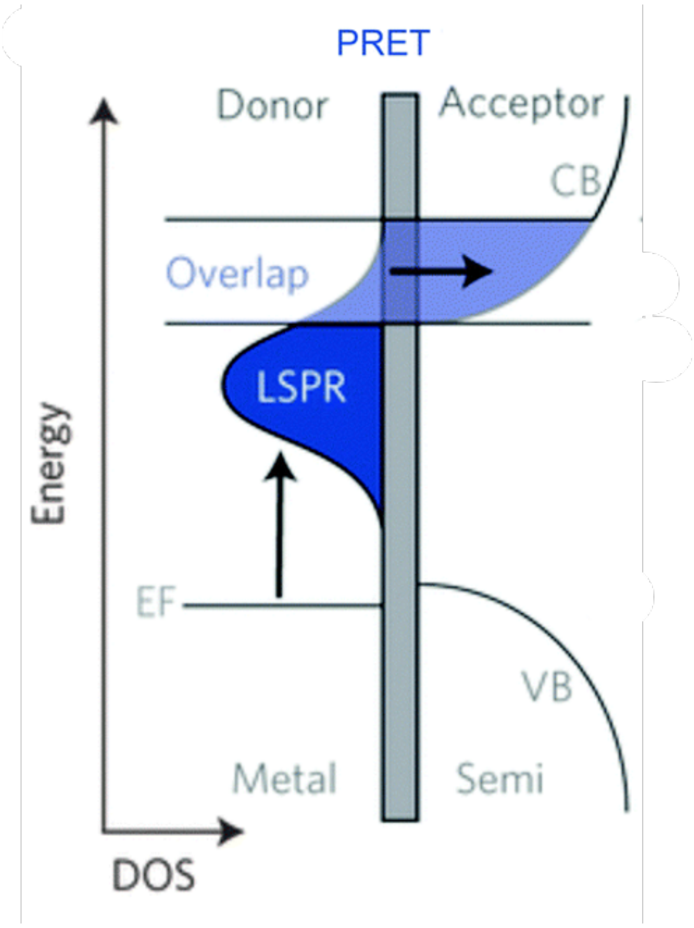

Figure 2.8: Schematic of PRET where resonant energy is transferred to the semiconductor molecule in the overlap region. Note that band alignment is not needed for this to occur.

PRET can be characterized by increased photocurrent when the conditions for hot electron transfer are not met (insulating layer and band alignment). Additionally, in the very specific case that the conditions for both PRET and hot-electron transfer are met, where there is alignment of the Fermi level as well as a spectral overlap in absorption, both PRET and hot-electron transfer can occur. [42]

Plasmonic Enhancement in Solar Cells

Plasmonic enhancement in current PV has been demonstrated by engineering the size, shape and composition of metallic nanostructures to achieve significant efficiency enhancement. Recently, Dabirian et. al simulated nanoparticles on top of a TiO_2 photoanode and observed a 40% increase in scattering with 700 nm Ag particles compared to a 2% increase with 100 nm Ag particles due to an increased ability at larger sizes to divert light at larger angles, thereby increasing the optical path length. [44] While initial research in plasmon-enhanced PV focused on spherical nanoparticles, recently increased efficiency enhancement has been observed with nanorods, nanocubes, core-shell nanostructures and other varied geometries which give rise to enhanced polarizability. These structures often allow for localized charge concentration at corners and edges which then leads to near-field enhancement as previously discussed. Figure 2.9 shows the improvement in absorbance and current density in dye-sensitized solar cells employing nanorods over nanospheres. [45, 46]

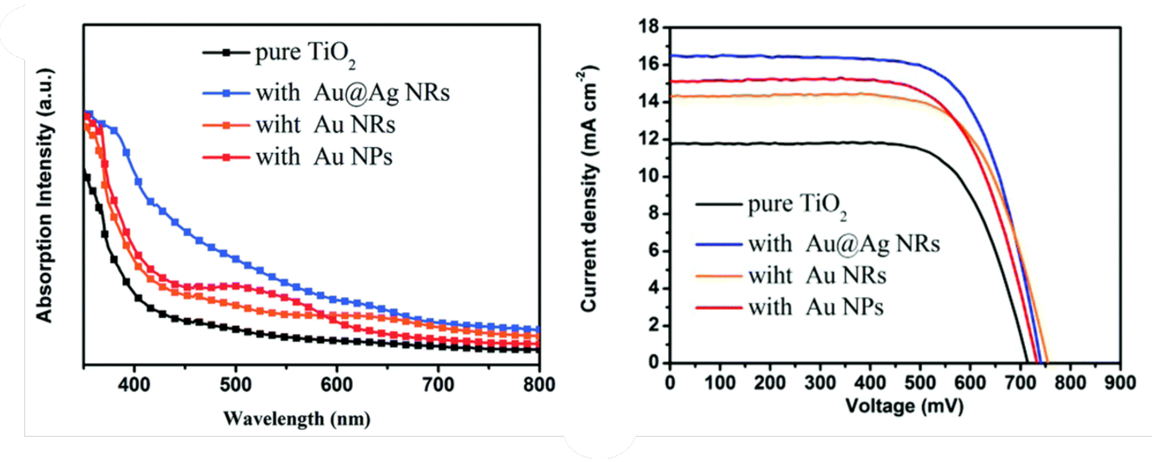

Figure 2.9: Absorption intensity of TiO$_2$ electrodes with Au and Ag nanoparticles incorporated and IV scans of nanoparticle-incorporated dye sensitized solar cells.

Nanoparticle composition has been successfully varied to produce optimal results in several PV systems. Au and Ag are most commonly used due to their superior radiative properties. While Au has higher optical losses than Ag, it also has higher stability, and both achieve LSPR in the visible light range while being simple to fabricate. [47] More recently, Al has also been studied due to its broad LSPR spectral tunability from 350-500 nm and low optical losses. [48] While Al has lower light trapping efficiency than Au or Ag, other benefits such as higher chemical stability and increased charge carrier separation have been observed. [49] As plasmon-incorporated PV systems showed increasing success, researchers have recently begun exploring the concept of plasmon-enhanced PPV. Carretero et. al performed FDTD simulations on Au, Ag and Al nanoparticles in PVSK cells made with MAPbI$_3$. [50] While only radiative effects were simulated, the results were intriguing as shown in Fig. 2.9. According to this simulation, Ag nanoparticles with 130 nm radius showed absorption higher than a PVSK-only film of 1000 nm thickness. Snaith et. al first attempted experimental incorporation of plasmonic nanoparticles in PPV in 2013, where SiO_2 coated Au nanoparticles mixed into an Al_2O_3 scaffold which improved photocurrent density by 14.5%. [51] This was attributed to a reduction in binding energy, which is the energy required to separate electron-hole pairs into free charge carriers and avoid recombination. In another study, significant spectral enhancement was observed by incorporating TiO_2 coated Ag nanospheres in an Al_2O_3/PVSK active layer, which increased device efficiency by 20%. [52] In this case, enhancement was not due to binding energy reduction but rather improved absorption from far-field scattering.

Chapter 3

Experimental methods

3.1 Sample preparation

This section discusses sample preparation and, where relevant, synthesis. Unless specified otherwise in the pertinent chapter, all samples are deposited on indium tin oxide (ITO) coated glass substrates. ITO-coated glass is preferable since it will not reflect or absorb light in spectroscopy measurements, and the ITO coating is conductive so the sample can be analyzed using scanning electron microscopy. The substrates are cut from a larger slab by scoring using a diamond cutter and metal ruler and gently breaking along the guide. The substrates used for the samples discussed in Chapters 4 and 5 are cut to approximately 1.5 cm × 1.5 cm while the large-scale LSC discussed in Chapter 6 is deposited on a substrate cut to 5 cm × 5 cm. The substrates are prepared for sample deposition by placing in a sample holder and sonicating first in deionized water, then acetone and finally isopropyl alcohol, with 15 minutes allocated to each step. They are then dried under a stream of oxygen and stored in a single layer in a closed petri dish until deposition.

3.1.1 Perovskite thin films

While similar in final chemical composition, the perovskite thin films outlined in Chapter 4 are prepared using different techniques and precursors from those in Chapter 5 due to differing priorities in optimal characteristics between the two projects, as well as changes in inventory and equipment availability.

PVSK thin films for luminescent solar concentrators

The films reviewed in Chapter 4 use various lead precursors for the perovskite halide, which is discussed in more detail within the chapter, combined with methylammonium iodide (MAI) as the cation source. The MAI is purchased from Luminescence Technology Corp. while the lead halide compounds and N,N-Dimethylformamide (DMF) solvents are purchased from Sigma-Aldrich. To purify the MAI, the MAI powder is mixed with 28.5 ml of anhydrous ethanol and 1.5 ml of anhydrous methanol and magnetically stirred in an oil bath at 60° for 2 hours until completely dissolved. The solution then continues to be stirred at room temperature with the addition of 150 ml of diethyl ether to re-crystallize the MAI powder, and then is filtered using filter paper. The resultant crystals are washed with diethyl either and the process is repeated until all MAI is purified and white in color. The purified MAI powder is then stored in a vacuum environment overnight to dry.

To prepare the film solution, the precursors are combined according to the following ratios: for $CH_3NH_3PbI_3$ prepared with PbI_2, 119 mg of MAI and 345 mg of PbI_2 are added to 750 μl of DMF; for $CH_3NH_3PbI_3$ prepared with $Pb(Ac)_2$, 314 mg of MAI and 250 mg of $Pb(Ac)_2$ are added to 750 μl of DMF; for $CH_3NH_3PbI_{3\text{-}x}Cl_x$ prepared with $PbCl_2$, 210 mg of MAI and 122 mg of $PbCl_2$ are added to 500 μl of DMF; and for $CH_3NH_3PbI_{3\text{-}x}Cl_x$ prepared with $PbCl_2$ and $Pb(Ac)_2$, 358 mg of MAI, 104 mg of $PbCl_2$ and 122 mg of $Pb(Ac)_2$ are added to 750 μl of DMF respectively. For each solution, the MAI is added first and sonicated until completely dissolved before adding the lead compounds. The solutions are then sonicated for 1 minute before stirring overnight in a N_2 glovebox. The films are prepared from the solution by spin-coating on the prepared substrates at 3000, 4000, 5000 and 6000 rpm for 30 s for each solution to achieve the range of thicknesses desired for study. In total, this will make 16 samples of varying composition and thickness. The samples are then annealed on a hot plate at 100–120°C until completely dry and darkened in color, which takes 30 min–2 h depending on the composition and thickness of the sample. Thinner samples and samples containing $Pb(Ac)_2$ require shorter annealing times due to a higher by-product evaporation rate, which is discussed in more detail in the chapter. The samples remain in the glovebox for the entire deposition and annealing process, after which they are removed and ready for characterization.

3.1.2 Perovskite quantum dots

Perovskite quantum dots were synthesized by our collaborators at University of California, Santa Cruz, Evan T. Vickers and his supervisor Jin Z. Zhang. $CH_3NH_3PbBr_3$ QDs were synthesized using a solvent reprecipitation method under ambient conditions. CH_3NH_3Br (80 μmol, 9.0 mg), $PbBr_2$ (0.20 mmol, 73 mg), benzoic acid (0.74 mmol, 90 mg), and 400 μL DMF was added to a borosilicate vial and the solution was sonicated until all solid dissolved. Then, benzylamine (0.10 mmol, 11 μL) was added, and the solution was sonicated again for 20 sec. 100 μL precursor solution was added at a medium rate to 5.0 mL toluene. The PQD solution was centrifuged at 4,000 rpm for 2 minutes and the brightly fluorescent liquid extracted. The liquid was further purified using cotton-plug filtration. This procedure was republished with permission from Ref. [53].

3.1.3 Perovskite/Au samples

Perovskite quantum dot samples made with Au nanoparticles were fabricated by either drop casting or dip coating. Drop casted samples were prepared by pipetting 200μL of 45 ppm AuNP solution (either 5nm or 10nm) in water from NanoPartz onto clean glass slides and annealing on a hot plate at 100° C until completely dry. Subsequently, 200μL of the previously described quantum dot solution was deposited on the dried and cooled (to room temperature) AuNPs and left to dry in air. The samples were then stored covered in a glovebox for several days while measurements were taken.

Dip coated samples were made by first preparing a 1 mM 1,2-ethanedithiol (EDT) in acetonitrile solution in order to facilitate ligand exchange. Clean glass slides are lowered first in the AuNP solution then slowly lifted out of the solution at a rate of approximately 1cm/s. The bottom of the slide is tapped gently on a paper towel to remove excess liquid. The slide is then rinsed in pure acetonitrile at the same dipping rate, then rotated 90° to ensure uniformity and the process is repeated 5 times. Once dry, the QDs are deposited similarly, using the EDT/acetonitrile solution in between QD layers.

3.2 Photoluminescence spectroscopy

Characterization of a material's optical properties rely on a thorough understanding of its light-matter interactions. Photoluminescence in semiconductors occurs when the material is exposed to incident light with an energy at or above the material's band gap that excites electrons into a higher energy state. When these excited electrons decay to their ground state, they spontaneously emit photons which we then measure as emission. Measurement of this emission can then reveal deeper material properties such as surface defect states, degradation or decomposition of the material or (in combaniation with absorbance) quantum yield. The following sections discuss the experimental details of the photoluminescence (PL) measurements provided in this work.

3.2.1 Steady-state photoluminescence spectroscopy

A steady-state photoluminescence measurement is generally performed by exciting a sample with a focused beam and collecting emission that is focused into a spectrometer. A schematic of the experimental setup used for the PL measurements provided in this thesis is shown in Fig. 3.1. The light source used a Supercontinuum laser system with an AOTF filter (SuperK) from NKT Photonics. The SuperK is wavelength and power tunable, which is important for optimizing excitation. Ideally, a sample should be excited above its bandgap but not at much higher energies, to prevent multi-excitonic processes from interfering with data as well as to avoid damage to the material. The laser light is collimated and then focused onto the sample, and the emission passes back through the path of the incident light. A beam splitter placed between the laser and the sample then redirects the emission into an objective that focuses into a spectrometer. Since the reflected laser light will also be redirected, a long pass filter is placed between the beam splitter and objective in order to filter out the reflected light and ensure that only emission is collected by the spectrometer. The spectrometer is then connected to a computer that analyzes the emission at each wavelength and provides an emission spectra. It is important to conduct these measurements in a dark room to avoid ambient light generating noisy spectras, and to connect the sample holders and spectrometers to 3D adjustable stages since signal optimization is very sensitive to slight position adjustments.

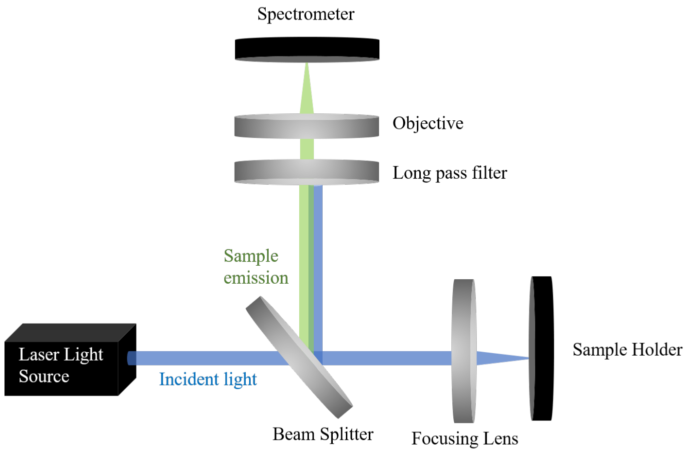

Figure 3.1: Diagram of experimental setup for steady-state photoluminescence.

3.2.2 Scanning photoluminescence spectroscopy

A scanning PL setup is made much the same way as steady-state, with the sample being mounted to an automated 3D stage controlled via LabView. Scanning PL allows us to observe the shifts in emission over a small area to understand the uniformity and possible defect areas of a sample and their nature. A step size (in length) for the x- and y-scale is input into the LabView program and a PL map is generated over the selected region of area. The step size is limited by the wavelength of the laser light utilized in the measurement, though the maps shown in this work are lower in resolution, with step sizes of several microns or higher.

3.2.3 Time-resolved photoluminescence spectroscopy

Time-resolved photoluminescence spectroscopy (TRPL) utilizes time-correlated single photon counting (TCSPC) to obtain a time-dependent histogram of emission from which we can extract recombination lifetime values. TRPL is a powerful and useful tool for distinguishing the nature of recombination processes as well as studying the charge transport properties of a material. TCSPC relies on excitation provided through a short laser pulse, after which the generated photons are collected by an avalanche photodiode. A schematic of the experimental setup for TRPL is provided in Fig. 3.2. The setup is similar to a PL setup, with an additional beam splitter used to allow the emission to be collected by both a spectrometer and the photodiode. While only the photodiode is necessary for the lifetime data, the spectrometer is useful to collect wavelength-dependent PL at the same spot for comparison as well as to help optimize the setup and overall emission counts.

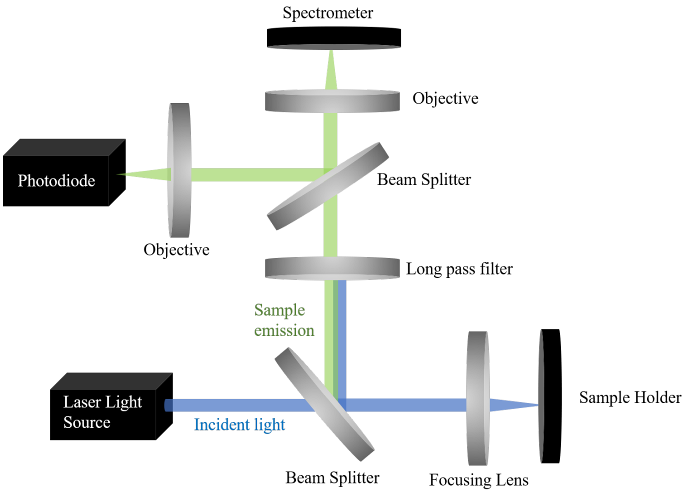

Figure 3.2: Diagram of experimental setup for time-resolved photoluminescence.

Because a single short laser pulse would not provide enough photon counts to get an accurate analysis, the average is taken across a series of pulses where the measured time interval is between the pulse and the detection of an emitted photon. The SuperK provides a synchronization signal which means the time at the pulse does not need to be measured by a trigger diode, and the time at the emission is measured by the photodiode. Fig. 3.3 provides an illustration of this measurement.

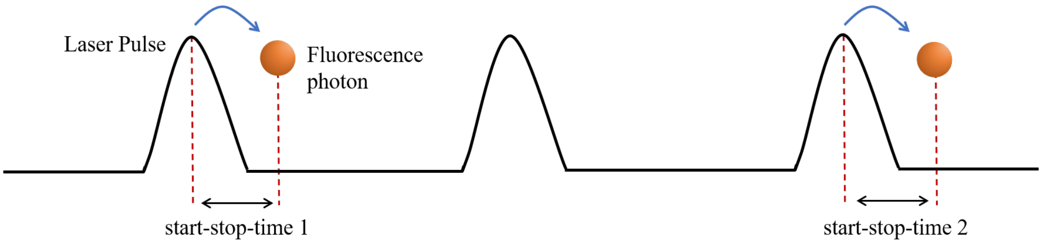

Figure 3.3: Illustration of start-stop times in time-resolved photoluminescence measurement using TCSPC.

When this measurement of counts at each time interval is repeated many times, the resultant histogram displays an exponential decay as shown in Fig. 3.4. This shape is a result of the probabilistic nature of this process, where at each time interval each excited molecule has a 50% probability of relaxation to the ground state, which would leave 50% of the molecules in the excited state. Since the intensity is determined by the photons emitted from this relaxation, the intensity decreases proportionally to the excited molecules, hence resulting in an exponential decay.

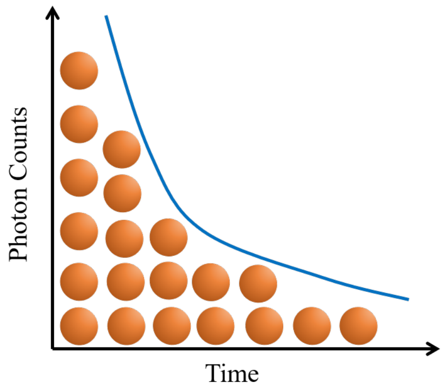

Figure 3.4: Histogram of counts during time-resolved photoluminescence measurement.

3.3 Ultraviolet-Visible absorption spectroscopy

In order to measure the absorption spectra of a material, ultraviolet-visible (UV-Vis) spectroscopy is employed. UV-Vis measures the sum of the absorbed and scattered light in a material by first measuring the incident light spectrum with no sample present. Once the reference measurement is collected, a sample is placed in the UV-Vis and a broadband light source is passed through to measure the transmitted light. The absorption is then defined as

$$A = \log \frac{I}{I_0} \tag{3.1}$$

where I_0 is the intensity of the incident light transmission and I is the intensity of the transmitted light. [54] The absorption spectra is then obtained by measuring over a range of wavelengths, and correcting the baseline from the reference measurement.

Chapter 4

Optimization and scalability of hybrid perovskite thin films as luminescent solar concentrators

4.1 Introduction

Luminescent solar concentrators (LSCs) were originally introduced as a cost-effective alternative to traditional photovoltaic systems. Historically, LSCs have employed a polymer or glass substrates doped with fluorophores, such as quantum dots or dye molecules, to act as waveguides for down-converted sunlight to be directed to solar cells attached at their edges.[20, 55, 33, 56] LSC-based solar cells have many advantages when compared with traditional solar cells, and one of the most important of these is their ability to absorb both direct and diffuse sunlight. This allows LSCs to be incorporated into otherwise difficult architectures, such as vertical surfaces,and reduced cost for large area coverage.[57, 21] Conventional optical concentration photovoltaic (CPV) technology uses concentrating optics to reduce solar cell area while maintaining high efficiency in order to commercially allow the use of higher efficiency and more costly solar cells relative to planar non-concentrated PV.[58] Typically, the CPVs employ Fresnel lenses or mirrors with single or dual axis tracking and have a typical concentration ration of 300–1000 for high concentration PV (HCPV). HCPV systems often utilize high efficiency, relatively expensive multi-junction solar cells such as GaInP/GaInS/Ge.[58] Efficiencies of commercially available CPV modules exceed 30%, with a Soitec model recently exhibiting 38.9% efficiencies at standard concentration.[59]

Luminescent materials typically used in LSCs should ideally possess high quantum yield (QY), broadband absorption, and emission that is spectrally-matched to the band gap of the attached solar cell. Since the concept was introduced, LSC research has encompassed a wide array of materials. The most commonly used fluorescent components investigated include organic dyes and semiconductor quantum dots such as CdSe/CdS, CdSe/ZnS and PbS.[60, 61, 33] The highest power conversion efficiency (PCE) to date is 7%, achieved in a dye-based LSC coupled to GaAs solar cells.[62] While this does not compare favorably with the performance of 1st and 2nd generation crystalline and thin film photovoltaics, it is close to the highest reported PCE of quantum dot-based solar cell.[63] The biggest hurdle that prevents LSCs from practical implementation is not efficiency but scalability, which arises from 'self-absorption' (SA) losses. In most materials, the spectral overlap of the absorption and emission bands results in the emitted light being re-absorbed by the material, and barring 100% QY, this results in further losses. There are two avenues to reducing SA: one is band gap engineering to induce a large spectral separation between absorption and emission bands, called Stokes shift[64]; the other is to leverage materials with higher QY.[60] There has been some success with designing quantum dots with almost no SA losses, and although they have allowed the formation of relatively large LSCs, they have not necessarily translated to high efficiency devices.[65, 60, 66] The best approach would therefore be to not focus on arresting SA alone, but to also invest in materials with high QY, which is the route we have taken.

Metal-halide hybrid perovskites (PVSKs) have been at the forefront of photovoltaic research for the past six years, owing to their rapidly improving PCE as thin film solar cells.[67] The highest reported value currently stands at 22.7% [68] compared to 22.9% for thin film calcogenide solar cells and 26.7% for Si crystalline solar cells. However, device stability remains a problematic issue, and success on that front has not kept up with advances in performance.[69] While recent perovskite solar cells have achieved stability under 1000 h of continuous illumination, this still falls far short of the 20-year lifetime expected for silicon solar cells.[70] However, PVSKs are unique materials tha have superior optical characteristics in conjunction with high carrier mobility and are highly suited for incorporation in LSCs as well as traditional solar cells.[71, 72] Typical materials used for downconversion in LSCs include lanthanides and nanophosphors, but these are not as easily synthesized as PVSKs.[73] While opaque thin films are generally not used in LSCs due to high self-absorption, in our prior work we observed that the high QY, broad absorption spectra, and large refractive index in hybrid PVSKs ($n = 2.5$) compensated exceedingly well for this shortcoming, achieving an impressive optical efficiency (η_{opt}) of 29%.[72] Additionally, they remained stable over a period of months under ambient conditions.[72] The flexibility of chemical composition of the hybrid PVSKs allows for many variations by using different halides (Cl, I, or Br) or even combinations of halides. Each of these composites have different quantum yields and absorption spectra, which create a very large phase space of parameters that will influence LSC performance.

While optimal morphology for PVSK solar cells has been well researched[74], LSCs prioritize different qualities. In this work, we investigate the roles of halide composition, morphology and film thickness in PVSK based LSCs, and report an impressive experimental optical efficiency of 34.7%. In addition, 3D Monte Carlo simulations based on the data predict the PVSK properties could allow LSCs as large as 1 m.

4.2 Experimental Procedure

Our PVSK thin films are synthesized following established protocols.[72] To systematically explore the phase space, we vary both film thickness and precursors, totaling sixteen different combinations. The solutions are prepared by adding purified (MAI) methylammonium iodide purchased from Luminescence Technology Corp. to N,N-Dimethylformamide (DMF) solvent, followed by the relevant lead halide compound, $PbCl_2$, PbI_2 or $Pb(Ac)_2$, all purchased from Sigma-Aldrich. The mixture is sonicated for one minute, and then stirred overnight in a N_2 glovebox. The films are prepared from this mixture by spin-coating on indium tin oxide (ITO) coated glass substrates at 3000–6000 rpm for 30 s to produce thicknesses ranging from 150 to 600 nm, followed by annealing on a hot plate at 100–120°C for 30 min–2 h. The annealing time is dependent upon the by-product evaporation rate, which is much faster for samples containing acetate, while samples containing iodide and/or chloride are on the slower end, taking upwards of an hour to anneal the thickest samples. The samples remain in the glovebox throughout the spin-coating and annealing process and are removed and exposed to ambient conditions only when ready for measurements. The thickness of each sample is measured using cross-sectional SEM imaging using FESEM (Zeiss, ULTRA-55) with secondary electrons as the signal type. Top-down SEM images are then taken of all the samples to observe surface characteristics. These films also undergo typical characterization including x-ray diffraction.[72, 75]

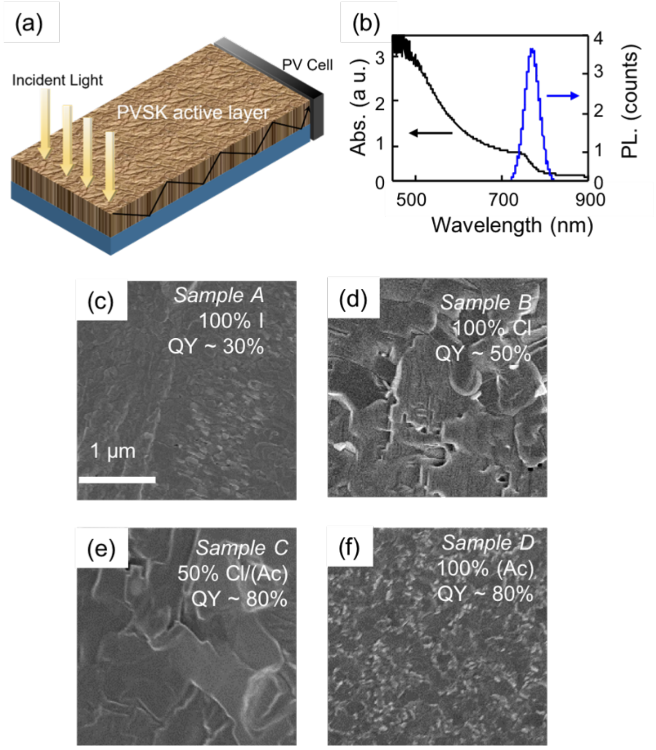

Figure 4.1: Spectral and surface characterization. (a) Schematic of an LSC with a PV cell attached at one edge. (b) Absorption and PL spectra of a typical PVSK thin film. (c–f) Scanning electron microscope (SEM) images for samples A–D. All films are 450 nm thick.

Fig. 4.1(a) is a schematic of our device architecture. The PVSK thin film forms the active material which absorbs normally incident sunlight and transmits the down-converted emission to standard silicon (Si) photovoltaic (PV) cells attached perpendicular to the surface along the edge. For optical efficiency measurements, we measured current from the Si cells in ambient sunlight with and without our LSCs and calculated optical efficiency using $\eta_{\text{opt}} = \frac{\mathrm{I_{LSC}\times A_{PV}}}{\mathrm{I_{PV}\times A_{LSC}}}$, where the geometric gain is defined as the ratio of the areas of the LSCs and PV cells attached at the edges and, considering the entire circumference, is 3.75 for our samples. Absolute QYs of thin films is a notoriously difficult measurement, especially given these are highly inhomogeneous polycrystalline samples. We therefore estimated QY using an Acton SP2300 spectrophotometer relative to a standard laser dye. Self-absorption (SA) is measured by collecting emission from the sample edge after exciting our thin films with a broadband white light source. By varying the pump-detector distance and measuring the resulting intensity drop in emission, we quantified the

SA loss. We also performed spatially resolved photoluminescence (PL) scans at normal incidence using a continuous wave laser source tuned to 408 nm.

4.3 Results

Fig.4.1(b) is a representative plot highlighting the broad absorption band and near infrared emission spectrum of one of the PVSK samples. Fig. 4.1(c)–(f) are scanning electron microscopy (SEM) images of a subset of our samples that highlight the differences caused by the different halide precursors during synthesis. The halide precursors (final compositions) for samples A–D are PbI_2 ($CH_3NH_3PbI_3$), $PbCl_2$ ($CH_3NH_3PbI_{3\text{-}x}Cl_x$), 1:1 mixture of $PbCl_2$ and $Pb(Ac)_2$ ($CH_3NH_3PbI_{3\text{-}x}Cl_x$), and $Pb(Ac)_2$ ($CH_3NH_3PbI_3$), respectively. Samples A and D are both pure halide PVSKs and have the same final composition, but as the SEM images show, the morphology is very different. The same is true for samples B and C, which are both mixed halide PVSKs. The use of different precursors influences the surface greatly, since each precursor produces different by-products that evaporate at varied rates.[74, 76] Faster evaporation rates lead to smaller grains and smoother surfaces.[74, 76, 77] Consequently, $PbCl_2$ tends to produce larger crystalline grains while $Pb(Ac)_2$ leads to smaller crystals but a smoother morphology, and these trends are supported by our SEM images. The effect of sample crystallinity on emission properties is a complex and slightly debated topic. Theoretical models show PVSK grain boundaries to be intrinsically benign relative to other polycrystalline materials[78], but experimental studies contend that they might act as trap sites, increasing non-radiative recombination.[79] The relative QY for A–D averaged over several samples of each type is noted in the figure as well, and indicate that the presence of $Pb(Ac)_2$ improves the yield.

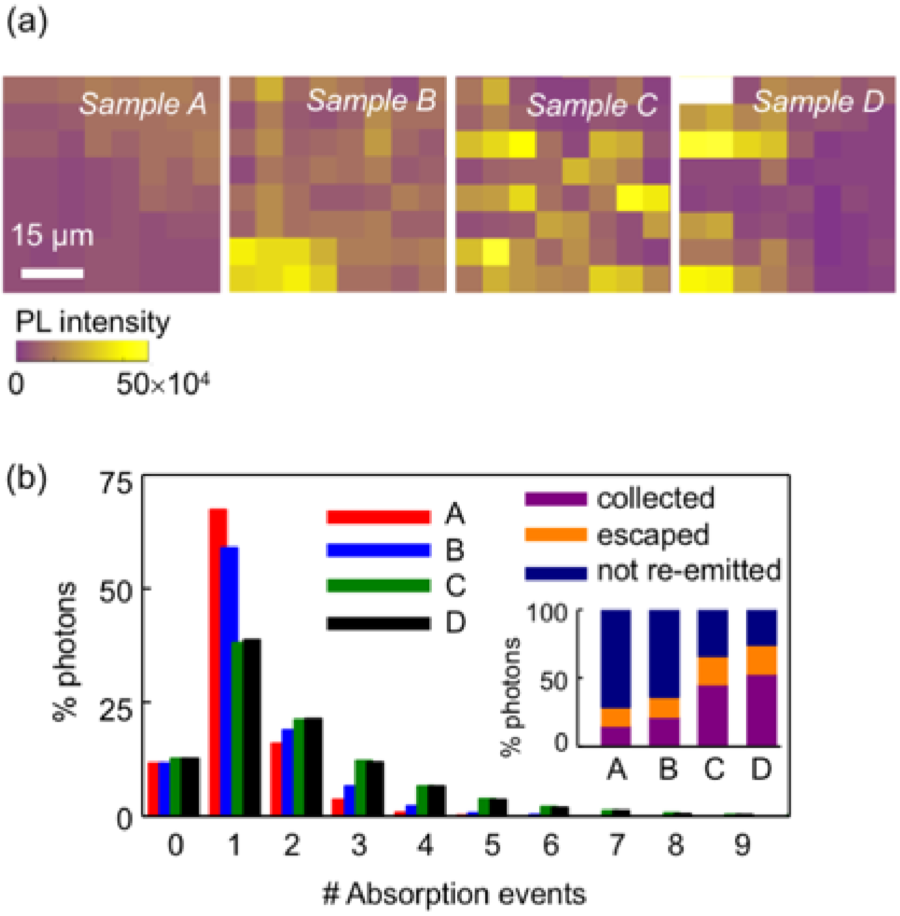

Figure 4.2: Comparison of optical emission and absorption. (a) Spatially-resolved PL intensity scans of 40 μm^2 areas of the samples. (b) Histogram comparing simulated percentage of photons undergoing absorption events in the samples with film thickness 450 nm. (*inset*) Relative proportion of photons collected, lost, and re-emitted.

Fig. 4.2 is a comparison of optical emission and absorption of the four samples. Fig. 4.2(a) is a set of spatially resolved scanning PL maps where the optical emission is collected at normal incidence. Integrating the emission over the scanned spatial area indicates sample A has the lowest PL count, sample B being next while samples C and D on average have the highest. This variation highlights the critical role of precursors in PVSK morphology and how that affects optical yield and characteristics. $PbCl_2$ in the precursors enhances crystallinity due to slow byproduct evaporation rate[74], which should reduce nonradiative recombination, while the presence of $Pb(Ac)_2$ is known to suppress the growth of large crystals, increasing the grain density and the sites of non-radiative losses through the proliferation of grain boundaries.[77] We incorporate the absorption and emission data from Figs.4.1 and 4.2 into 3D Monte Carlo simulations that use the model of a box-shaped LSC, with dimensions of 5 cm × 5 cm × thickness t, whose top surface points toward the sun, the bottom is attached to a perfect mirror, and the side edges are covered by solar cells. The normally incident radiation is sampled from the terrestrial solar spectrum[20] and assumed to be Lambertian. Propagation distances inside the material are based on inverting the Beer-Lambert law[80] using measured absorbance and emission spectra. Photons absorbed by the material are probabilistically emitted isotropically based on the chance of non-radiative recombination and the material emission spectra. Photons striking the top surface are probabilistically reflected or transmitted based on Fresnel reflectance with a measured substrate refractive index of $n=1.7$ to account for the ITO coating (the results are similar using $n=1.5$). Snell reflection is employed on the bottom surface and on reflected photons at the top surface. Photons are monitored until they strike a side edge where they would be collected by a solar cell, escape back through the top surface, or are lost by non-radiative routes and therefore not re-emitted. We also monitor the number of times each photon is absorbed. In Fig. 4.2(b) the main bar plot charts the percentage of photons undergoing a specific number of absorption events in the four samples. ‘0’ represents incidents photons that are not absorbed at all, which account for 12–15% of the incident excitation. This proportion is consistent for all PVSKs irrespective of composition given the film thicknesses are the same. Beyond that, sample A has the highest absorbance, as noted by the largest proportion of ‘1’ (first) absorption event. It also has the lowest probability for more absorption events (‘#’>1) which ought to translate to low self-absorption (SA) losses. The inset compiles the proportions of photons that escape, are not reemitted, and are collected by solar cells at the edges. There is a clear monotonic increase in the percentage of collected photons from samples A–D that follows the QY trend of Fig.4.1(c)–(f) and suggests that high QY is indeed capable of overcoming SA losses. Additional details about the simulations are available in the supplementary document.

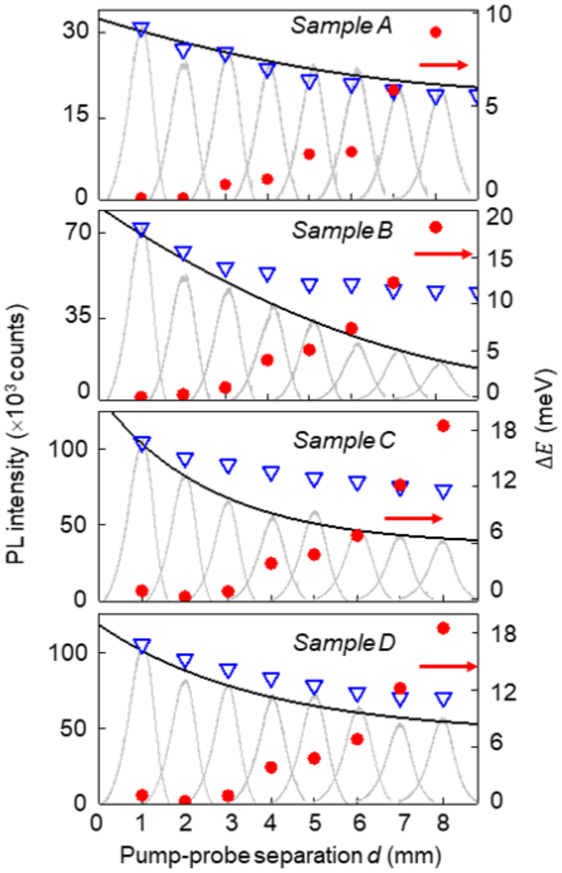

Figure 4.3: Estimating self-absorption. PL spectra (gray curves) at increasing pump-probe separation shown to demonstrate emission intensity loss along the length of the LSCs designed from samples A–D. Peak intensity as function of the same separation is superposed in black on the spectral curves. Simulated percentage of photons collected (downward triangles) and emission peak energy shift (filled circles) with varying *d* are also shown for every sample.

We obtain a quantifiable measure of SA losses in the LSCs in Fig.4.3. The samples are excited normally with a white light source focused down to a 1 μm spot and PL is collected from the edge as the separation between excitation and collection *d* is varied by laterally translating the excitation spot. The PL curves (gray) of samples A–D show a steady drop in emission intensity with increasing *d*, as is expected given the QY is always less than 100%. In addition to intensity reduction, the process of re-absorption and re-emission results in an overall red-shift of the PL spectra.[72] We track the peak emission wavelength with *d* and plot the difference between it and the d=0 value as ΔE(circles) for each sample. At first glance it appears as though sample A has the best outcome, where the intensity reduces by less than 40% and the spectral shift is 8 meV; but the initial low PL due to the small QY puts it at a disadvantage. Sample B has the worst SA losses, and despite having a higher QY, sample C does not seem to translate that to superior SA properties. Sample D possesses the best combination of high QY and acceptable SA losses with the emission falling to 43% as the light traverses the sample length. This is still a substantial loss compared to other active materials[78], but not unexpected, considering the active medium is a continuous film, not comprised of discrete dopants. Further, the trend in the edge emission data of sample D indicates the intensity drop is leveling off, which is a positive attribute that could allow for scaling up of device dimensions.

We investigate the scalability aspect next through simulations. Based on the same LSC model used to generate the data in Fig. 4.2(b), we calculate SA losses in the LSCs. In this exercise, the distance that a photon travels until it is absorbed is determined using Beer-Lambert's law, based on the (corrected) absorption spectrum (see [69] for details). Once absorbed, the probability of this photon to be reemitted is the QY. If re-emitted, the red-shifted wavelength and the emitted intensity is sampled from the emission spectrum and the photon's direction is chosen randomly assuming isotropic emission. The calculated spectrally-integrated emission intensities as functions of d are plotted in Fig. 4.3 for samples A–D (triangles) normalized to the experimental results. There is good agreement between simulation and data for samples A and D, both of which are pure iodide films. The same is not the case for the mixed halide $CH_3NH_3PbI_{3-x}Cl_x$ samples, B and C. Revisiting Fig. 4.2(a), we can see that the PL maps of samples B and C have more of a checkerboard pattern, becoming spatially non-uniform because of the larger grains that are typical when $PbCl_2$ is used as a precursor. This inhomogeneity is not incorporated in this simple fitting model. However, as this model seems to work well in samples A and D with smaller grains, we extend the scope of the MC simulations to larger sample sizes. Once again, the calculations use the measured absorption and emission data. However, there is significant SA in all the samples, which, for $\lambda > 760$ nm, is "in the noise" of the absorption data. To address this issue, we take one measured PL value, corresponding to $d = 1$ mm, and use it to fit the tail of the absorption spectrum as exponentially decreasing beyond 760 nm. We then use this "corrected" absorption spectrum to generate the computational results for larger LSCs and plot the calculated percentage of photons at varying d in Fig. 4.4.

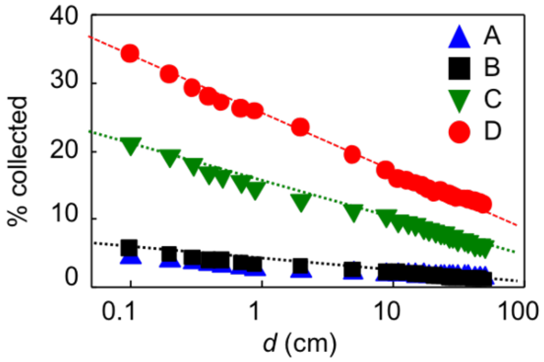

Figure 4.4: Simulation of self-absorption in large scale LSCs plotted with excitation-collection separation.

Not surprisingly, samples A and B prove unsuited for use in realistic devices, with less than 5% of total incident light available for collection beyond 1 cm from the point of illumination. Samples C and D show more encouraging trends and the latter has 28% of the initial emission available for collection after traversing 100 cm. For comparison, the largest LSC so far, with a size 100 cm has shown an optical efficiency of 4.5%. The other parameter that affects LSC performance is the film thickness. PVSKs are advantageous in that they absorb very efficiently over the entire visible spectrum, but highly absorptive thick films also ratchet up the SA. Solar cell design focuses on ultrathin films ($<$ 150 nm) to maximize carrier extraction, but concentrators do not have this restraint. Experimental optical efficiency η_{opt} values are summarized in Fig. 4.5.

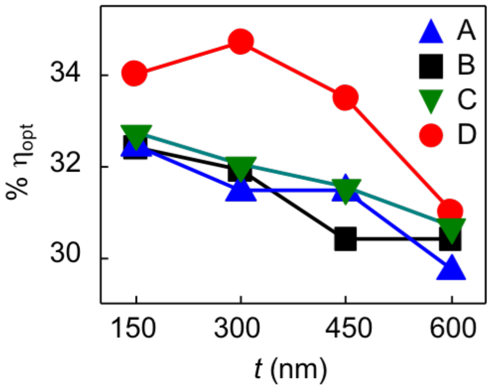

Figure 4.5: Optical efficiency experimentally measured for LSCs as a function of film thickness in the various composites.

Surprisingly, experimental η_{opt} is very similar for samples A–C that have disparate QYs. Sample D, where there is a small non-monotonicity, with the highest η_{opt} of 34.7% observed at t=300 nm followed by reduced efficiency with increasing thickness. Taken together, this leads us to the conclusion that thin films synthesized using 100% $\mathrm{Pb(Ac)_2}$ precursors such as sample D behave most like homogenous active media. This is expected from the SEM images that confirm a smooth morphology. Samples A–C behave atypically, which we attribute to the morphological non-uniformity that lowers QY and negates any gain from enhanced absorption.

4.4 Conclusion

Perovskite thin films are shown to be excellent candidates for LSCs. By optimizing the morphology and thickness of the sample, we can achieve a maximum optical efficiency of 34.7%, with a minimum of 29.7%. This is a result of perovskite materials having overall high quantum yield, large Stokes shift, and large refractive index. The incorporation of acetate makes a smooth film that allows light to travel to the sample edges with minimal self-absorption, resulting in a high-efficiency LSC. While thicker samples increase absorption, the increased self-absorption is detrimental in all except the highest quantum yield samples, giving better results with thinner films. For most samples, film thickness of 150 nm achieved the best performance. Additionally, the emission wavelength is favorable for silicon photovoltaics, showing promise for incorporation into large scale photovoltaic systems. While our results reveal the critical role of $\mathrm{Pb(Ac)_2}$ in sample synthesis, intriguingly, all samples show high η_{opt}, once again confirming the suitability of hybrid PVSKs as LSC material. MC simulations corroborate our results, suggesting that SA losses can be overcome by high QY and allow for scaling up of devices. While commercialization of perovskite LSCs will require improvements in device stability, toxicity and synthesis, existing technical options can address these to a large extent. For example, encapsulation of the device in glass would provide resistance from eroding due to moisture and oxygen, while also preventing exposure to a lead environment. Further improvements can be made to the device by engineering the substrate and the geometry for improved optical efficiency. Our investigations also highlight the issues that affect accurate evaluation of PVSK materials, chief among them being how QY is measured and incorporated into device modeling.

As the discrepancy between the calculated and experimental results in Fig. 4.2 highlights, global QY estimation is an unreliable estimate of nonradiative recombination losses in a sample with a morphology as inhomogeneous as observed in these materials. Correlations between morphology and emission at high spatial resolution as we have shown here is an important step towards providing an accurate prediction, not only as concentrators, but also as solar cells.

Acknowledgements

This research was supported by funds from the National Aeronautics and Space Administration (NASA) grant no. NNX15AQ01A.

Appendix A. Supplementary material

Supplementary data to this article can be found online at
https://doi.org/10.1016/j.solener.2019.03.042.

Chapter 5

Emission enhancement of hybrid perovskite quantum dots and thin films via plasmonic Au nanoparticles

The tunable optoelectronic properties and high quantum efficiency of quantum dots (QDs) make them intriguing species for study in a wide array of applications ranging from photovoltaics to biosensing. [81, 82, 83] As hybrid metal-halide perovskites have recently emerged as highly desirable semiconductors for photovoltaic applications due to their superior optical properties, perovskite quantum dots (PQDs) are now gaining increasing attention for a variety of applications including potential light emitting diodes (LEDs), solar cells and lasing due to their ease of tunability, low cost and high quantum yield. [84, 85]

While the emission wavelength is easily tuned by changing the composition and size of a QD, emission intensity is more difficult to control. Since many applications of QDs benefit from maximizing the emission intensity of QDs, a successful strategy for providing emission enhancement has been through localized surface plasmon effects provided by coupling between the semiconductor nanocrystal and metallic nanoparticles. Surface plasmon resonance occurs when photons at resonance frequency interact with a plasmonic metallic nanostructure, causing the free electrons to collectively oscillate. In the vicinity of semiconductor nanoparticles, this could facilitate energy transfer, increase absorption events for the semiconductor, or alter the radiative and nonradiative dynamics of recombination for the material's excitons after absorption. [86]

In this chapter, we examine the emission enhancement by different sizes of gold nanoparticles (AuNPs) on $MAPbBr_3$ PQDs. We see strong emission enhancement as well as lifetime increase for PQDs coupled with 5nm AuNPs, while we observe PL quenching and lifetime decrease for all PQDs with 10nm AuNPs. We then discuss the opportunity for further understanding of the nature of these interactions.

5.1 Optical characterization and emission enhancement

Since stability is one of the largest limitations in all perovskite materials, attempts at passivation of surface defects extend to PQDs as well. The PQDs used in these experiments are synthesized by our collaborators at UC Santa Cruz with unique ligands containing benzylamine (BZA) and benzoic acid (BA) intended to slow moisture degradation and enhance stability. [53] Fig. 5.1a shows the absorbance and PL spectra of these $MAPbBr_3$ PQDs. The peak absorption and emission wavelengths for these PQDs are 520 and 525nm respectively, as expected for bromide-based perovskites, with a long (>6 months) shelf life in solution. They display a narrow PL band with a full-width-half-maxima of 27 nm.

The transmission electron microscope (TEM) image in Fig. 5.1b shows the PQDs to average 6.3 ± 1.2 nm in diameter, with the lower insets showing an average lattice spacing of 0.28 nm. The upper inset shows x-ray diffraction (XRD) measurements whose peaks confirm the composition to be $MAPbBr_3$.

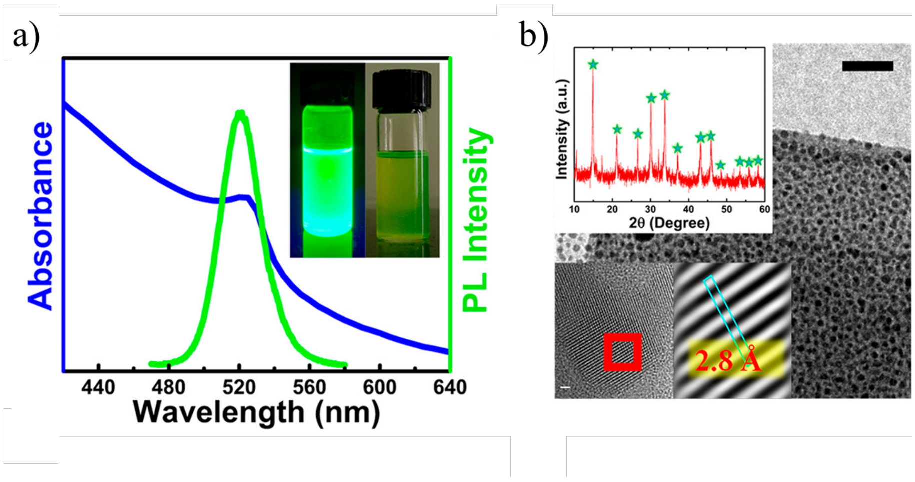

Figure 5.1: a) UV-Vis Absorption and PL spectra for BZA-BA-$MAPbBr_3$ PQDs, inset shows fluorescence in solution at room temperature. b) TEM image of QDs (scale bar 50 nm). The lower left inset is HRTEM image with lattice spacing (scale bar 1 nm), and the upper left inset is XRD pattern with symbols assigned to the cubic phase. Reprinted with permission from [53].

To test plasmonic effects on these PQDs, we used a 45ppm in water solution of spherical gold nanoparticles (AuNPs) obtained from NanoPartz. Since plasmonic effects are highly size-dependent, we prepare separate samples using AuNPs of 5 nm and 10 nm to observe the size dependence of this interaction. We prepared samples by first drop-casting 200 μL of the AuNP solution onto clean glass slides and annealing on a hot plate at 100°C. Once the slide is completely dry and cooled to room temperature (so as not to harm the PQDs with high temperatures), 200 μL of the PQD solution is drop casted directly onto the dried AuNPs and the slide is dried in air at room temperature until ready for measurements.

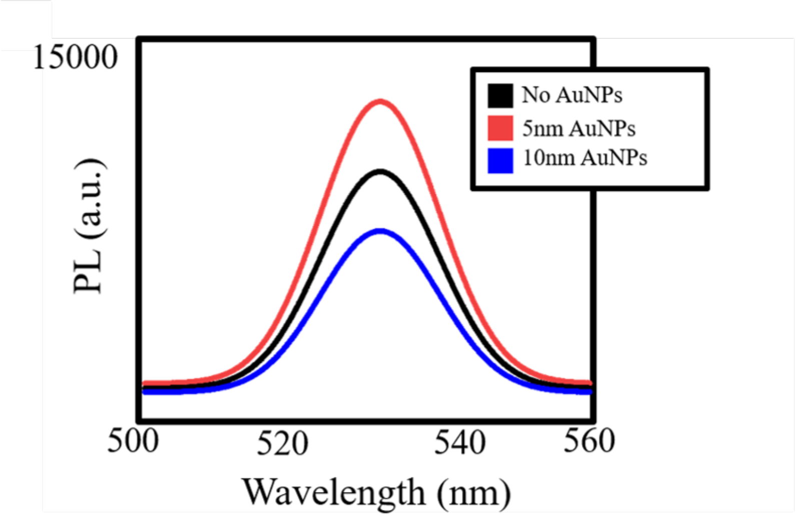

Figure 5.2: PL curves for drop-casted PQDs showing emission enhancement when coupled with 5 nm AuNPs and PL quenching when coupled with 10 nm AuNPs.

Fig. 5.2 shows PL curves of PQDs alone compared to PQDs drop-casted on 5 nm and 10 nm AuNPs. We observe an impressive 30% emission enhancement when the PQDs are coupled with 5 nm AuNPs, but 26% PL quenching when using 10 nm AuNPs, suggesting a strong size dependence of this interaction. This is particularly surprising because generally, larger metallic nanostructures are expected to be strong scatterers, so we would expect to see some emission enhancement with the larger AuNPs just from increased far-field scattering of the PQD emission. One possibility could be that while the smaller AuNPs are able to increase absorption in the PQDs through enhancement of the localized incident electric field, the 10 nm AuNPs are not spectrally suited to provide this absorption increase, but are also not large enough to effectively scatter emission, thus only existing as a rough surface between the substrate and PQD layer which produces defect sites and blocks emission. Another possible explanation is nonradiative energy transfer between the larger AuNPs and PQDs. Kim et al. showed an increase in PL quenching of CdSe QDs as surface denisty of adjacent AuNPs increased due to energy transfer from the QDs to the AuNPs, suggesting that this quenching mechanism is highly dependent on the surface provided by the AuNP layer. [87] Other examples of PL quenching by AuNPs through undesirable energy transfer are also supported by literature. [88, 89, 90]

However, the distance between the semiconductor nanoparticle and plasmonic nanoparticle is also known to be a crucial factor in emission intensity in a plasmon-semiconductor system. [90, 91] For this reason, we attempt to increase the enhancement seen in the PQD/5nmAuNP samples by drop-casting PQDs on a gold-patterned substrate. By carefully controlling the distance between AuNPs embedded into a silicon substrate, we can avoid clustering and potentially increase emission enhancement.

mnn

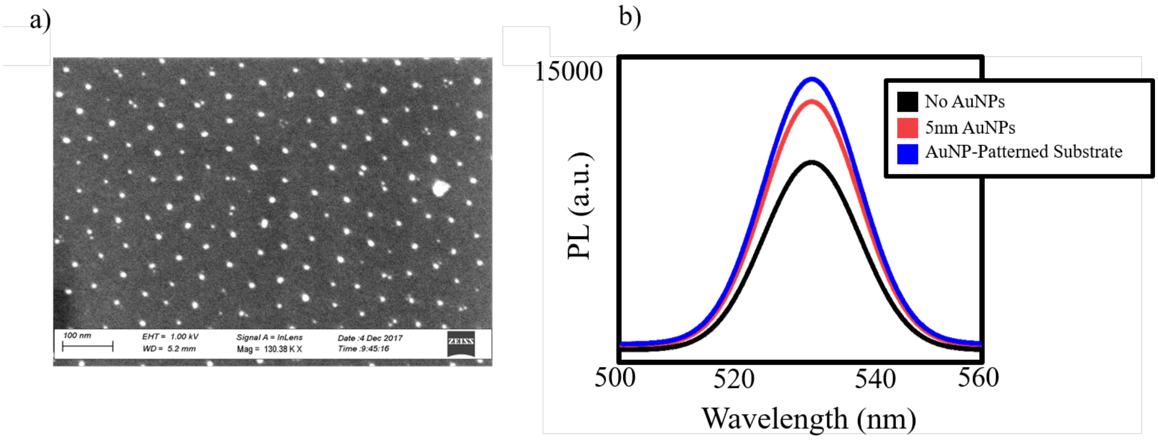

Figure 5.3: a) SEM image of patterned Au substrate (scale bar is 100 nm). b) Emission enhancement for PQDs via patterned substrate and drop-casted 5 nm AuNPs.

The Au-patterned substrates were prepared by spin-coating a mixture of poly(styrene-b-2-vinylpyridine) and $HAuCl_4$ in toluene followed by U-V-Ozone treatment at 150°C for 20 mins in O_2 environment. The resultant AuNPs measure on average 6.5 nm in diameter, and their size and separation can be tuned using block copolymer chains. Fig. 5.3a is an SEM image of the patterned substrate that shows uniform spacing between AuNPs. Fig. 5.3b compares emission enhancement of PQDs by drop-casted 5 nm AuNP and Au-patterned substrates. Emission enhancement increases by an additional 11% relative to drop-casted Au, providing further evidence of a strong dependence on spacing and density in plasmon-PQD interactions.

Despite displaying impressive optical properties, the Au-patterned substrates prove difficult to deposit uniform films on, as attempting to dip coat PQDs on them resulted in uneven films with large regions of non-adherence. This combined with their more involved synthesis process make them non-ideal candidates for the large-scale LSCs studied in the following chapter, where an important consideration for scalable LSCs is ease of fabrication.

5.2 Lifetime measurements

The probability of a luminophore emitting a photon is proportionally related to the photon mode density, or intensity of the localized electric field. [92] The complete photoluminescence process can be thought of as a combination of the excitation process, which is directly affected by the incident field and the local environment, and the emission process, which is directly influenced by the radiative and non-radiative decay rates. A plasmon in the vicinity of this luminophore can then enhance the emission by either increasing the excitation rate (by enhancing the incident electromagnetic field) or increasing the PL quantum yield (by increasing the radiative decay rate). [93]

The excitation rate Γ_{exc} is proportional to the plasmon-enhanced incident field intensity $E_{exc}(\omega)$ as

$$\Gamma_{exc} \propto |pE_{exc}(\omega)|^2 \tag{5.1}$$

where p is the transition dipole moment and ω is the transition frequency. [94] The plasmonic enhancement via this effect is then greatest when the LSPR wavelength overlaps with the material's *absorption* band. [95, 96] On the other hand, increasing the material's quantum yield is most effective when the resonance wavelength overlaps with the material's *emission* band. [97, 98] The total emission rate Γ can thus be written as

$$\Gamma = \Gamma_{exc} \left(\frac{\gamma_r}{\gamma_{nr} + \gamma_r} \right) \tag{5.2}$$

where γ_r is the radiative decay rate and γ_{nr} is the non-radiative decay rate. [94] Most plasmonic enhancement contributions can thus be attributed to either an increase in Γ_{exc} as increased light absorption, or an increase in γ_r as increased radiative decay. Interestingly, our PQD/AuNPs show evidence of *both* effects, possibly because of the close proximity between the PQD's absorption and emission bands.

Fig. 5.4 shows lifetime data for PQDs alone, PQDs with drop-casted 5nm AuNPs, and PQDs on the Au-patterned substrate. The average lifetime is calculated from a bi-exponential decay fit according to the following equation:

$$I(t) = A_1 \text{exp}(-t/\tau_1) + A_2 \text{exp}(-t/\tau_2) \tag{5.3}$$

where τ_1 and τ_2 are the lifetimes and A_1 and A_2 are their amplitudes. The average lifetime is then determined by

$$\tau_{ave} = \frac{\tau_1 A_1 + \tau_2 A_2}{A_1 + A_2}. \tag{5.4}$$

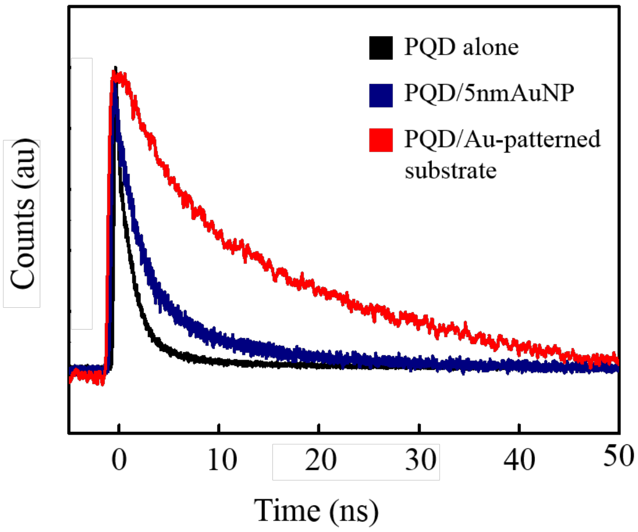

Figure 5.4: TRPL showing lifetimes of PQDs alone, PQD/5nmAuNP sample and PQD/Au-patterned substrate sample. Lifetime increase is prominent for patterned substrate, indicating strong dependence of enhancement on spacing.

The PQDs alone show an average lifetime of 9.60 ns, while the PQDs on drop-casted 5nm AuNPs and patterned substrates show increased lifetimes of 14.63 ns and 23.53 ns respectively. These results suggest that an increase in the radiative decay rate is partly responsible for the emission enhancement observed in the PQDs. This can be explained by considering that an increased local electric field due to plasmonic resonance will then alter the optical density of states in the QD, resulting in an increase in the decay rate. [99] Steady-state analysis has determined that the radiative decay rate of a molecule depends on the total dipole moment, not just the molecular dipole. [100] Since the localized electric field can produce an additional induced dipole, it has been observed that the radiative decay rate of a semiconductor particle in a plasmon-induced electric field will display an increased radiative decay rate. This enhancement has been shown to be sensitive to the separation distance r between the plasmon and semiconductor, as the enhanced electric field is expected to decay proportionally to r^{-6}. [99] This can explain why once again the patterned substrate shows higher enhancement than drop-casted

AuNPs. Biteen et al. observed significant increase in radiative decay lifetimes for silicon nanocrystals coupled with Au plasmons, while observing a decrease in lifetime enhancement as Au plasmons increased in size. [98]

In agreement with these trends, we also observe a decrease in lifetime as we increase AuNP size. Fig. 5.5 shows spatially resolved maps of lifetime and PL measurements taken simultaneously on samples containing no AuNPs, 5nm AuNPs and 10nm AuNPs. The average lifetimes across the region for no AuNPs, 5nm AuNPs, and 10nm AuNPs are 9.50ns, 14.80ns and 8.44ns respectively. The maps containing AuNPs show clear correlation between regions of increased PL and increased lifetime (in the sample containing 5nm AuNPs), as well as correlation between regions of decreased PL and decreased lifetime (in the sample containing 10nm AuNPs). This provides further evidence suggesting an increase in non-radiative recombination rate in PQD samples containing 10nm AuNPs, as we see little evidence of decreased PL without decreasing lifetime as well. Since there is no correlation between the lifetime and PL maps in the sample without AuNPs, we can confirm that the AuNPs are responsible for both the emission and lifetime effects.

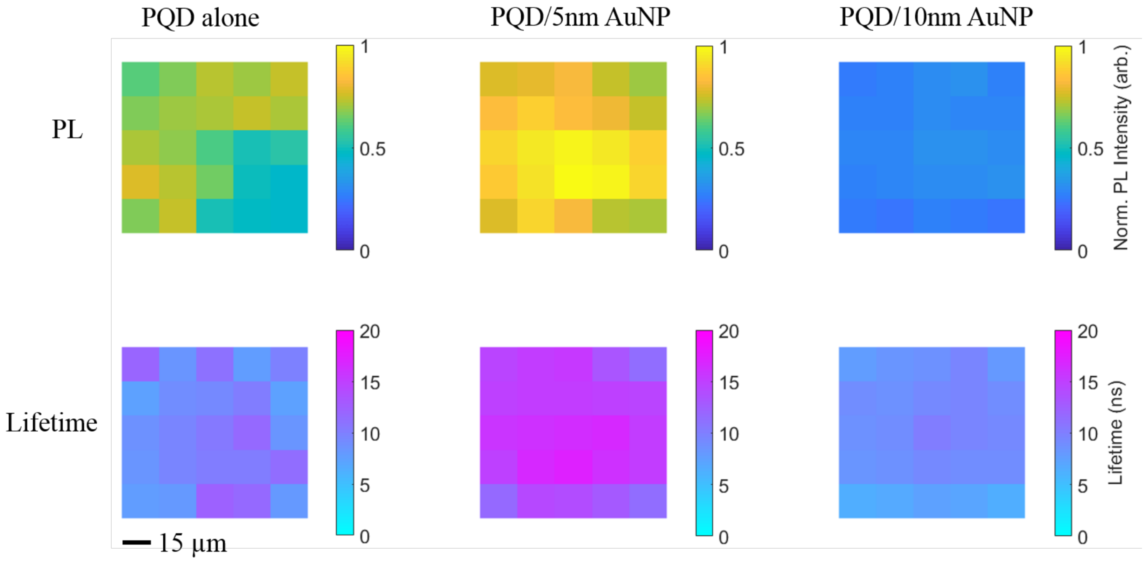

Figure 5.5: Spatially resolved maps showing PL and average lifetime for three samples: PQDs alone, PQDs with 5nm drop-casted AuNPs, and PQDs with 10 nm drop-casted AuNPs. The corresponding locations on the PL and Lifetime maps for each sample are identical locations taken at the same time with the same excitation. The step size between locations is $15\mu m$. The three PL maps have the same normalized scale bar, while the three lifetime maps also share the same scale, to easily compare the enhancement/quenching results. There is visible correlation between PL enhancement/quenching and lifetime increase/decrease for the 5nm/10nm AuNPs respectively.

5.3 Extent of plasmonic contributions

We observe clear plasmonic enhancement of both emission and lifetime of PQDs with smaller gold nanoparticles, whether drop-casted or on a patterned substrate. This enhancement can be attributed to an increased localized electric field that both increases the absorption rate and increases the radiative decay rate, resulting in a large increase in emission intensity. While the enhancement effects can be understood as plasmonic near-field enhancement, further investigation into the exact nature of the quenching effects could yield interesting results.

The decreased lifetime of PQDs when coupled with 10nm AuNPs suggests that the decrease in emission would be a direct result of coupling between the PQDs and AuNPs rather than simply decreasing absorption of incident light by the PQDs. Plasmon resonant energy transfer is observed when the resonance energy in the collective electron oscillations of the metallic nanoparticle spectrally matches the transition energy of excitons in a nearby semiconductor, and thus results in a shortening of lifetime as the energy transfer occurs on a much smaller timescale than the radiative decay process. [101] This interaction is particularly spatially sensitive, as interfacial contact could result in losses due to hot-electron transfer. [102] Adding a spacer layer between the 10nm AuNPs and the PQDs could then instead facilitate charge separation and prove useful for photovoltaics. [103]

More rarely, in the strong coupling regime, plasmon-exciton pairs can exhibit hybrid modes that allow for very fast energy transfer. [104] These plasmon-exciton pairs, often called plexcitons, are identified by a Fano resonance or Rabi splitting in the absorption spectrum, characterized by the emergence of hybrid modes when the coupling strength of the plexciton exceeds the dissipation energy. [105] Achieving evidence of the strong coupling regime in plasmon-PQD pairs without the use of microcavities would prove to be an incredibly interesting and useful research topic for the future, with many potential applications in lasing and photocatalysis. [105] Many of these ultrafast processes can be measured using a combination of transient absorption spectroscopy and time resolved differential transmission to probe the charge carrier dynamics on a femtosecond scale. [106]

This is to say that the PL quenching and lifetime decrease observed in the 10nm AuNP/PQD system should not necessarily be considered a negative result. While we pursue applications of the emission enhancement in PQD/5nm AuNP systems for luminescent solar concentrators in the following chapter, further investigation into the nature of plasmon-QD interaction and dynamics of the 10nm AuNP/PQD samples could provide scientifically rich results with many applications outside the scope of this work.

Chapter 6

Large area hybrid perovskite quantum dot luminescent solar concentrators with Au nanoparticles

Our work thus far has revealed perovskite thin films to be excellent candidates for luminescent solar concentrators, and perovskite quantum dots to exhibit significant photoluminescence enhancement when coupled with plasmonic gold nanoparticles. Optimizing this enhancement through control of plasmon concentration and film uniformity can then allow us to extend these results into novel LSC devices. As discussed in Chapter 2, LSCs incorporating quantum dots have been extensively studied and continue to hold some of the highest reported LSC efficiencies to date due to their wide absorption efficiencies and tunable emission.

Perovskite quantum dots, therefore, should be obvious candidates for LSCs since PQDs possess a distinct advantage for LSCs over most quantum dots: a relatively high quantum yield. However, extensive research on PQD-based LSCs has been largely discouraged due to the large overlap between the absorption and emission bands, suggesting too high self-absorption. In 2017, Zhao et al. attempted to overcome this barrier by designing LSCs based on mixed-halide $CsPb(Br_{0.2}I_{0.8})_3$ PQDs which have a much larger Stokes shift than single halide PQDs. [107] This LSC reached a maximum optical efficiency (η_{opt}) of 2$\%$ for a 9cm x 9cm device. In 2018, the same group incorporated these mixed-halide PQDs into a tandem LSC device with carbon dots, achieving η_{opt} of 3.05$\%$ for a 10cm x 10cm device. [108] While these results prove that material engineering is a viable path to successful PQD-based LSC devices, alternative avenues for single-halide PQDs remained largely unexplored.

In March of 2020, Lu et al. incorporated TiO_2 nanoparticles into a a $CsPbBr_3$ PQD solution which was then molded into a polymer matrix, proposing a dual transmission mode LSC based on both fluorescence and TiO_2 scattering of light.

[109] While the TiO_2 nanoparticles are not plasmonic, this work nonetheless supports our idea of incorporating metallic nanoparticles into PQD-based LSCs to enhance its optical properties. The $CsPbBr_3/TiO_2$ LSCs displayed less competitive efficiencies, however, exhibiting 2.62% power conversion efficiency for a 5cm x 5cm LSC, which decreased to 1.82% for a 20cm x 20cm LSC.

In this chapter, we successfully fabricate a single halide PQD-based LSC incorporating plasmonic gold nanoparticles that achieve a competitive η_{opt} of 2.86% for a 10cm x 10cm device. By optimizing the concentration of 5nm AuNPs and synthesizing uniform devices through dip coating, we maximize emission enhancement while limiting self-absorption. Our device incorporating AuNPs exhibits a maximum PLQY of 77%, compared to an identical device with no AuNPs showing PLQY of 68%. Aside from the high efficiency, an important advantage of this work relative to similar current research is the ease of fabrication. Tandem and molded devices are significantly more complex to synthesize than dip coated layers. If one of the main goals of LSCs is to provide an affordable and reasonable means of improving photovoltaics on a commercial scale, then developing simplified and scalable methods becomes an important consideration.

6.1 Optical characterization

As discussed in Chapter 4, film uniformity is a crucial factor in limiting self-absorption of incident light through an LSC waveguide. QDs have an advantage over thin films as their discrete nature allows for natural separation with no grain boundaries to create trap sites, but uneven distribution on a substrate can still lead to losses through self-absorption in highly concentrated areas or diffusion losses in highly diluted areas. Thus, we employ a simple dip-coating procedure to ensure uniform PQD coverage. The samples are synthesized by first preparing a 1 mM 1,2-ethanedithiol (EDT) in acetonitrile solution in order to facilitate ligand exchange. ITO substrates are lowered first in the AuNP solution then slowly lifted out of the solution at a rate of approximately 1cm/s. The samples are then rinsed in pure acetonitrile at the same dipping rate, then rotated 90° to ensure uniformity and the process is repeated 5 times. Once dry, the PQDs are deposited similarly, using the EDT/acetonitrile solution in between QD layers.

The emission intensity is not only sensitive to spacing between PQDs, but also to the spacing between the AuNPs and PQDs. Since the enhanced local electric field decays exponentially, close proximity is necessary between the PQD and plasmon. [94] However, if the PQD is *too* close to the AuNP, the exciton pair can nonradiatively tunnel to the AuNP and result in energy loss. Therefore, to achieve maximum emission enhancement it is necessary to optimize the spacing between the AuNPs and PQDs. We do this by finding the optimal concentration of the AuNP solution to be dip-coated.

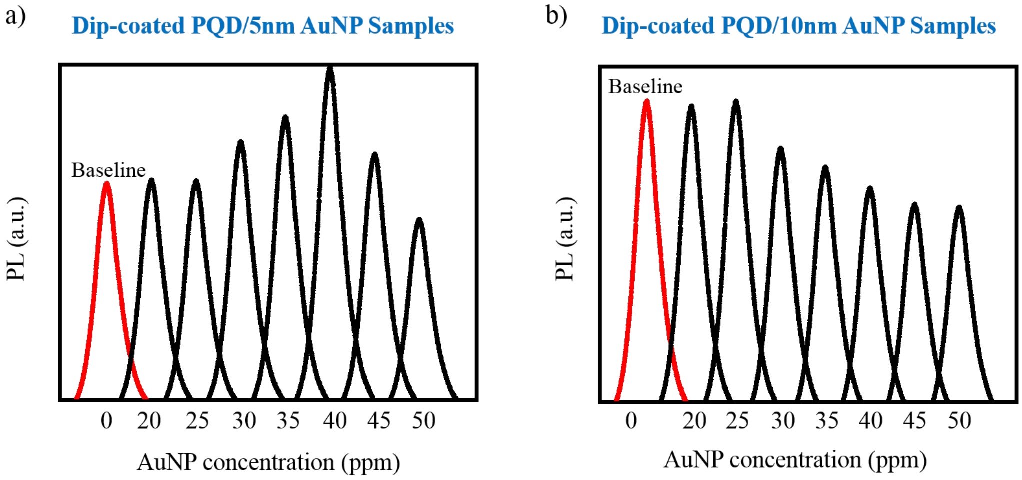

Figure 6.1: Photoluminescence curves of 5nm (a) and 10nm (b) AuNPs dip-coated with perovskite quantum dots as AuNP concentration is varied. Baseline curve of dip-coated PQDs with no AuNPs is shown in red.

Figure 6.1a shows the emission enhancement as a function of 5nm AuNP concentration. Samples at low concentrations show no evidence of plasmonic interaction, as emission stays nearly identical to the baseline (no AuNPs). At very low concentrations, only a few PQDs are within range of AuNP coupling. Increasing the concentration increases the percentage of PQDs coupled to AuNPs, resulting in emission enhancement. As the concentration exceeds the optimal level, however, the emission enhancement decreases and eventually quenches below the baseline level due to an increase in nonradiative recombination. We find the optimal 5nm AuNP solution concentration to be 40 ppm.

Although we observed no emission increase in PQDs drop-casted with 10nm AuNPs, the possibility exists that the emission and lifetime decrease is due entirely to a suboptimal concentration of AuNPs leading to nonradiative energy transfer. To test this, we perform similar experiments with dip-coated PQDs while varying the concentration of 10nm AuNPs as shown in Fig. 6.1b. At lower concentrations, the emission remains around the baseline intensity as in Fig. 6.1a, but increasing concentration only decreases the emission. This indicates that emission quenching is the result of plasmonic interaction, rather than a byproduct of suboptimal interaction.

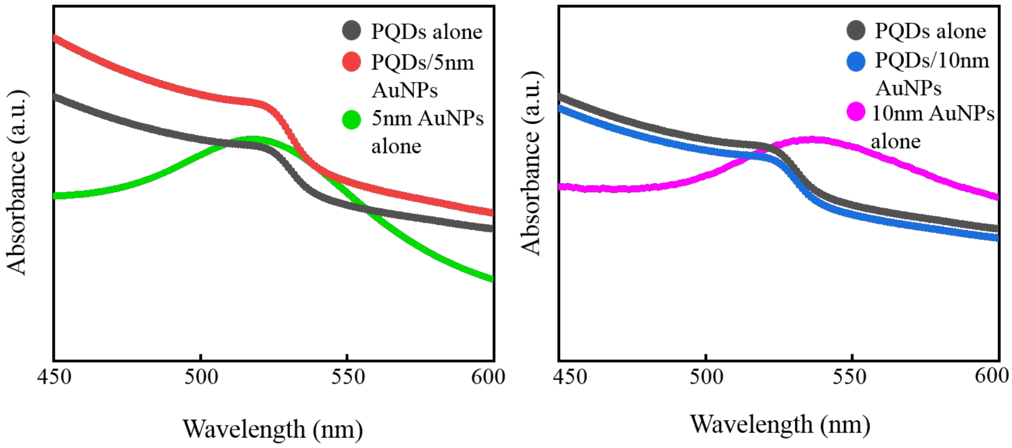

Figure 6.2: Absorption spectra for PQDs with 5nm and 10nm AuNPs compared to absorption for AuNPs alone.

In the previous chapter, we examined the contribution to lifetime increase due to plasmonic enhancement of the localized electric field in the vicinity of PQDs. We now examine the contribution of this field enhancement to the PQD absorption. Figure 6.2 shows absorption spectra for PQDs with and without AuNPs, overlaid with absorption spectra of the AuNPs alone. As expected, we observe an increase in PQD absorbance with the addition of 5nm AuNPs. The addition of 10nm AuNPs results in a negligible decrease in absorption, indicating that the absorption is also not responsible for the 10nm AuNP/PQD plasmonic interaction. Notably, the absorption peak of 5nm AuNPs aligns closely with the PQD absorption peak, whereas the 10nm AuNP absorption peak is much farther. This could explain why the 5nm AuNP/PQD interaction includes both absorption and lifetime enhancement and a significant absorption increase, while the 10nm AuNP is not spectrally suited to increase PQD absorption.

6.2 Optical efficiency

Once our synthesis procedure was optimized, we successfully produced a large-scale 10cm x 10cm LSC by dip-coating the optimal 40ppm AuNP solution followed by the PQD solution. Figure 6.3b displays a photograph of this LSC after annealing, showing uniform even coverage with the PQD solution shown adjacently. As a control, an identical 10cm x 10cm LSC with dip-coated PQDs and no AuNPs was also synthesized. Fig. 6.3a shows the emission enhancement for the large scale LSC using a white light source. We observe emission enhancement of 35% relative to the control sample, which is 5% higher than the enhancement shown for drop-casted PQDs and AuNPs from the previous chapter.

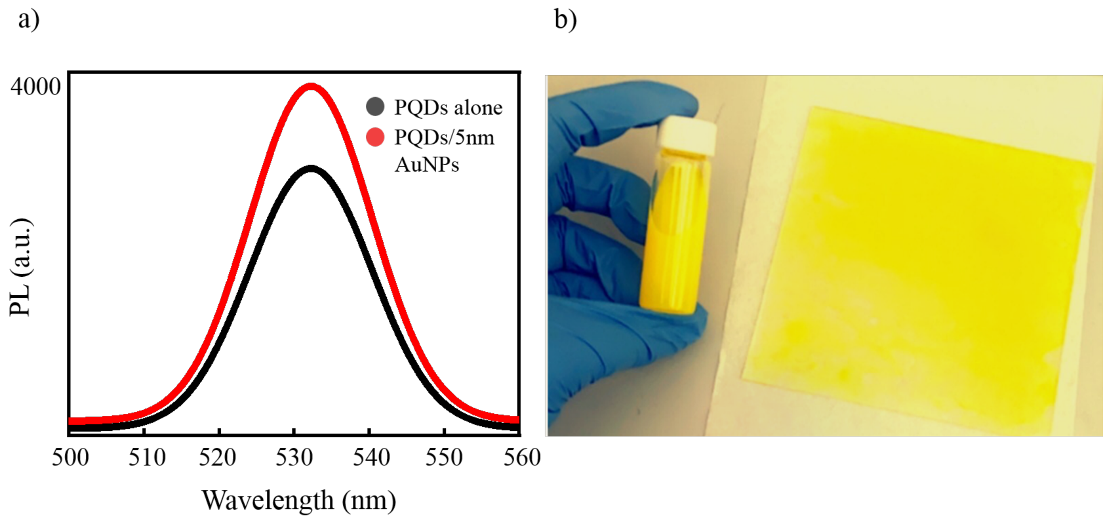

Figure 6.3: a) Photoluminescence enhancement and b) photograph of large scale 10 cm x 10 cm PQD/5nm AuNP LSC. PL increases by 35% relative to identical sample with no AuNPs. PQD solution is shown alongside dip-coated LSC showing uniform coverage over a large area.

We measure optical efficiency by measuring current from a standard Si PV cell in ambient sunlight with and without our LSCs and calculate optical efficiency using $\eta_{\text{opt}} = \frac{\mathrm{I}_{\mathrm{LSC}}\times \mathrm{A}_{\mathrm{PV}}}{\mathrm{I}_{\mathrm{PV}}\times \mathrm{A}_{\mathrm{LSC}}}$, where the geometric gain is defined as the ratio of the areas of the LSCs and PV cells attached at the edges. We report an optical efficiency of 2.87% for our large-scale LSCs, which have a gain factor G of 50. For comparison to our work in Chapter 4, samples measuring 1.5cm x 1.5cm with G = 3.75 show η_{opt} = 58%. The large-scale control LSC with no AuNPs, meanwhile, only exhibits η_{opt} = 1.72% for the same G = 50, indicating that the AuNP contribution is significant in improving optical efficiency.

Figure 6.4 compares these results with those of recently reported LSCs. Colloidal inorganic quantum dots were chosen for their high Stokes shift, with reported optical efficiencies of 1% for CdSe/CdS and PbS/CdS QDs, 1.15% for CdSe/CdPbS QDs and 2.86% for Si QDs. [64, 110, 111, 112] While CuInSSe/ZnS QDs reported a higher efficiency of 3.2%, this was also for a smaller gain factor. [113] While our thin films from Chapter 4 showed a high optical efficiency of 29%, they were also for smaller samples with G of only 3.75. The previously mentioned mixed halide PQDs reported higher optical efficiency and gain over all these inorganic QDs with a η_{opt} of 2% and G of 11.25. [107] Without engineering a large Stokes shift, our samples outperformed these mixed halide PQDs with η_{opt} of 2.87% and G of 12.5. Only the tandem C-dot/PQD LSC device has reported a higher efficiency at this size, but implementing a tandem structure could increase the efficiencies of our devices as well. [108] Thus, we successfully demonstrate the engineering of competitively efficient PQD LSCs utilizing plasmonic enhancement.

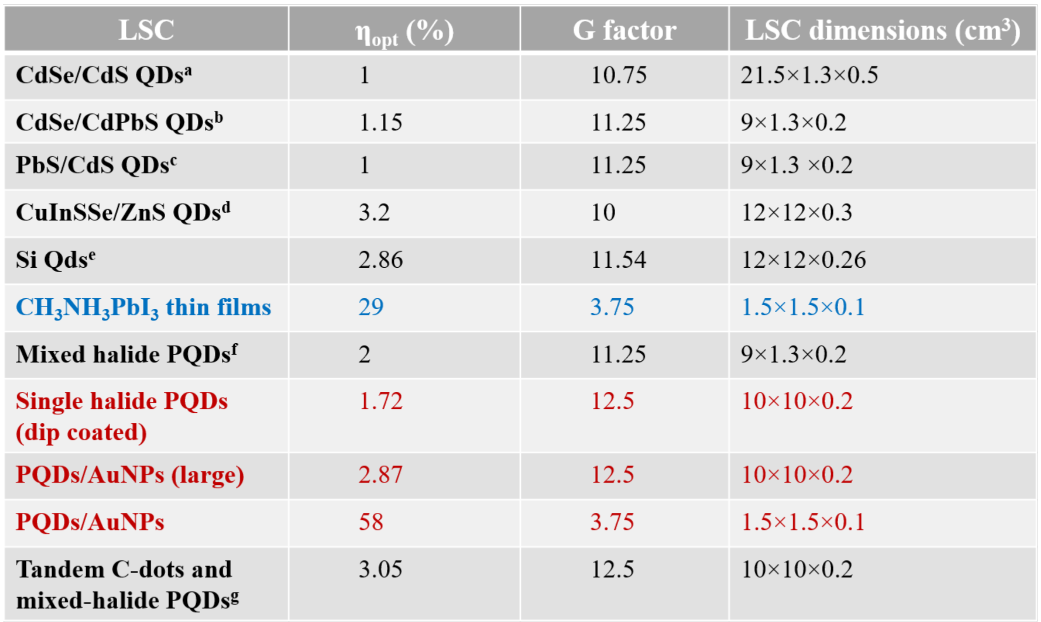

LSC	η_{opt} (%)	G factor	LSC dimensions (cm^3)
CdSe/CdS QDs[a]	1	10.75	21.5×1.3×0.5
CdSe/CdPbS QDs[b]	1.15	11.25	9×1.3×0.2
PbS/CdS QDs[c]	1	11.25	9×1.3 ×0.2
CuInSSe/ZnS QDs[d]	3.2	10	12×12×0.3
Si Qds[e]	2.86	11.54	12×12×0.26
$CH_3NH_3PbI_3$ thin films	29	3.75	1.5×1.5×0.1
Mixed halide PQDs[f]	2	11.25	9×1.3×0.2
Single halide PQDs (dip coated)	1.72	12.5	10×10×0.2
PQDs/AuNPs (large)	2.87	12.5	10×10×0.2
PQDs/AuNPs	58	3.75	1.5×1.5×0.1
Tandem C-dots and mixed-halide PQDs[g]	3.05	12.5	10×10×0.2

Figure 6.4: Table showing optical efficiencies, gain factors and dimensions for several most recent LSCs. This chapter's work is highlighted in red, while Chapter 4's work is highlighted in blue. Obtained from references [a][64], [b][110], [c][111], [d][113], [e][112], [f][107] and [g][108].

6.3 Self-absorption measurements

A natural concern would be that the absorption enhancement provided by the AuNPs would also lead to an increase in self-absorption, thereby reducing the LSC efficiency, but our self-absorption measurements show this is not the case. We measure self-absorption over the lateral sample size while increasing the distance between the excitation spot provided by the focused white light source, and the spectrometer collecting the side edge emission. Figure 6.5 shows the normalized emission intensity at 1cm intervals over the length of the sample. The result is compared to that of the large-scale control sample to determine whether the AuNPs negatively impact the self-absorption.

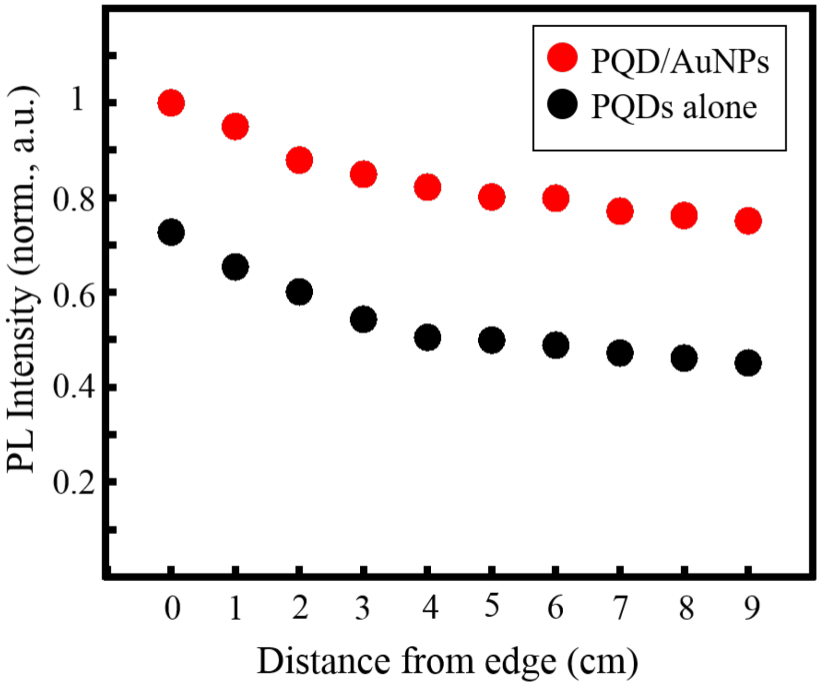

Figure 6.5: Self absorption measured on large-scale LSC using white light source with emission collected at edge.

We observe an emission decrease as expected, however, the emission intensity of the PQD/AuNPs sample only drops to 77.4% of its maximum intensity. The control meanwhile, drops to 79.2% of its maximum intensity, indicating that there is very slight increase in self-absorption when the PQDs are coupled to AuNPs. More significantly, however, is the fact that at the farthest point away from the collection area, the LSC made with AuNPs still had a higher emission than the *maximum* emission of the LSC with no AuNPs. Thus, it becomes apparent that the emission increase provided by the AuNPs outweighs the downside of potential self-absorption increase. This is due in part to the increase in quantum yield provided by the AuNPs; as observed in our work with thin films, the PLQY affects the self-absorption of a sample more than the overall absorption.

These $MAPbBr_3$ PQDs were selected for this project in part because of their impressively high quantum yield. To accurately determine a PLQY for dip-coated samples on ITO substrates, we utilize an integrating sphere with a 450nm laser input to determine absolute PLQY. We measure a PLQY of 68% for our dip-coated PQDs, which increases to 77% with the addition of AuNPs. The AuNP contribution to the increased QY as discussed in the previous chapter can be attributed to the increased radiative decay rate resulting from an increased optical density of states in the PQDs.

With these results, we successfully demonstrate the synthesis of a uniform, large-scale PQD-based LSC enhanced by AuNPs. We obtain an optimal AuNP concentration of 45ppm and employ dip-coating to create uniform and highly efficient films. We demonstrate η_{opt} of 2.87% for a 10cm x 10cm area device with PLQY of 77%. The addition of AuNPs exhibits absorption, emission and PLQY enhancement of PQDs while suffering minimally from an increase in self-absorption. The self-absorption measurments indicate potential for scaling up future devices for commercial applications.

These results are competitive with some of the highest currently reported LSC efficiencies without the need for Stokes shift engineering. Increasing the Stokes shift through generating a mixed-halide PQD or tandem device therefore remains a possibility to further improve the efficiency, but careful consideration must be made to the effects of the plasmonic enhancement. The small Stokes shift in our devices allows an overlap of the plasmon resonance with both the absorption and emission bands of the PQDs, which may not be possible with a larger separation. Acheiving a delicate balance between maximizing plasmonic enhancement and optimizing the material's optical properties would therefore be necessary to achieve more efficient devices.

Furthermore, device stability is a large and oft ignored concern when considering the viability of any perovskite device. Our PQDs have good long-term photostability (>3 months), but like all perovskite devices are prone to degradation with prolonged exposure to moisture and oxygen. [72] Encapsulation could prolong the device usage lifetime with minimal impact on efficiency. Additionally, a reflective surface utilized as a substrate would allow for a more efficient waveguide, thereby increasing the LSC's optical efficiency. While improvements to stability and efficiency will be necessary to reach commercial viability, these results remain promising for pushing perovskite materials to the forefront of LSC research.

Chapter 7

Conclusions and Outlook

This work provides insight into the potential of hybrid perovskite materials for solar applications via detailed optical characterization. Combining material engineering with a variety of spectroscopy methods, we have demonstrated perovskite thin films and quantum dots as successful candidates for luminescent solar concentrators, as well as other optoelectronic applications.

Although usually not considered for LSCs due to high self-absorption rates, PVSK thin films were shown to be efficient LSC devices due to an overall high quantum yield, large Stokes shift, and large refractive index. By optimizing the morphology and thickness of $CH_3NH_3PbI_3$ perovskite, the films acheived a maximum optical efficiency of 34.7%. Incorporating acetate allowed formation of smoother films that resulted in lower self-absorption and high quantum yield, while depositing thinner samples reduced the re-absorption rate of light traveling through the film. The optimal thickness was found to be 150nm for a spin-coated film, where the decreased absorption was offest by lower self-absorption. Additionally, Monte Carlo simulations tracking the progression of light through the LSC waveguide and estimating the proportion of output photons suggested that the high QY is sufficient to overcome self-absorption in scaled-up devices.

In addition to PVSK thin films, perovskite quantum dots were also examined as an emergent material for optoelectronic devices. In particular, the role of plasmonic interaction between metallic gold nanoparticles and hybrid $MAPbBr_3$ perovskite quantum dots was investigated. Optical characterization through emission, lifetime and spatially resolved photoluminescence measurements provided insight into the effect of plasmon resonance on deposited PQDs. Examining interactions between PQDs and 5nm, 10nm and patterned AuNPs illustrated the strong dependence of size and spacing in plasmon interaction. PQDs coupled to 5nm drop-casted AuNPs exhibited 30% emission enhancement and 4ns lifetime increase relative to PQDs with no AuNPs, while PQDs coupled to substrates patterned with similarly sized AuNPs exhibited 40% emission enhancement and 14ns lifetime increase. On the other hand, PQDs coupled to 10nm AuNPs showed a 26% decrease in emission intensity with a 2ns lifetime decrease.

The significant emission enhancement demonstrated by AuNPs when coupled to PQDs suggested that these PQDs could then be excellent LSC candidates. Competitively efficient large-scale LSCs were synthesized via dip-coating, acheiving a maximum optical efficiency of 2.87% for 10cm x 10cm devices with high quantum yield. Optimization of AuNP concentration allowed for ideal spacing between plasmon and quantum dot, with the highest emission enhancement acheived by 40ppm AuNP concentration. The addition of 5nm AuNPs increased PQD emission, absorption and quantum yield without increasing self-absorption significantly.

This work demonstrates the potential of hybrid perovskites for a range of optical applications, particularly in solar energy, due to their unique optical properties. Building off this work by more deeply examining the role of plasmon resonance in the 10nm AuNP and PQD interaction could provide illuminating insight into several nonradiative phenomena. Furthermore, improving on device efficiency, stability and toxicity in PQD and thin film PVSK LSCs could allow hybrid perovskite materials to eventually reach commercial viability as successful solar energy devices.

References

[1] OECD/IEA. *Key World Energy Statistics 2015*. Ed. by IEA.

[2] Mark Z. Jacobson and Mark A. Delucchi. “Providing all global energy with wind, water, and solar power, Part I: Technologies, energy resources, quantities and areas of infrastructure, and materials”. In: *Energy Policy* 39.3 (Mar. 2011), pp. 1154–1169. DOI: `10.1016/j.enpol.2010.11.040`.

[3] V.M. Fthenakis and H.C. Kim. “Photovoltaics: Life-cycle analyses”. In: *Energy Policy* 85.8 (Aug. 2011), pp. 1609–1628. DOI: `10.1016/j.solener.2009.10.002`.

[4] Anders Hagfeldt et al. “Dye-Sensitized Solar Cells”. In: *Chemical Reviews* 110.11 (Nov. 2010), pp. 6595–6663. DOI: `10.1021/cr900356p`.

[5] Masafumi Yamaguchi, Tatsuya Takamoto, and Kenji Araki. “Super high-efficiency multi-junction and concentrator solar cells”. In: *Solar Energy Materials and Solar Cells* 90.18-19 (Nov. 2006), pp. 3068–3077. DOI: `10.1016/j.solmat.2006.06.028`.

[6] Nam-Gyu Park. “Organometal Perovskite Light Absorbers Toward a 20% Efficiency Low-Cost Solid-State Mesoscopic Solar Cell”. In: *The Journal of Physical Chemistry Letters* 4.15 (July 2013), pp. 2423–2429. DOI: `10.1021/jz400892a`.

[7] Martin A. Green. “Corrigendum to ‘Solar cell efficiency tables (version 49)’[Prog. Photovolt: Res. Appl. 2017; 25:3-13]”. In: *Progress in Photovoltaics: Research and Applications* 25.4 (Feb. 2017), pp. 333–334. DOI: `10.1002/pip.2876`.

[8] Tomas Leijtens et al. “Stability of Metal Halide Perovskite Solar Cells”. In: *Advanced Energy Materials* 5.20 (Sept. 2015), p. 1500963. DOI: `https://doi.org/10.1002/aenm.201500963`.

[9] Martin A. Green, Anita Ho-Baillie, and Henry J. Snaith. “The emergence of perovskite solar cells”. In: *Nature Photonics* 8.7 (June 2014), pp. 506–514. DOI: `https://doi.org/10.1038/nphoton.2014.134`.

[10] Ivo Borriello, Giovanni Cantele, and Domenico Ninno. “Ab initio investigation of hybrid organic-inorganic perovskites based on tin halides”. In: *Physical Review B* 77.23 (June 2008). DOI: `https://doi.org/10.1103/PhysRevB.77.235214`.

[11] Andrei Buin et al. “Materials Processing Routes to Trap-Free Halide Perovskites”. In: *Nano Letters* 14.11 (Oct. 2014), pp. 6281–6286. DOI: `https://doi.org/10.1021/nl502612m`.

[12] Ilya Grinberg et al. “Perovskite oxides for visible-light-absorbing ferroelectric and photovoltaic materials”. In: *Nature* 503.7477 (2013), pp. 509–512.

[13] Jarvist M Frost et al. “Atomistic origins of high-performance in hybrid halide perovskite solar cells”. In: *Nano letters* 14.5 (2014), pp. 2584–2590.

[14] Fan Zheng et al. “Rashba spin–orbit coupling enhanced carrier lifetime in CH3NH3PbI3”. In: *Nano letters* 15.12 (2015), pp. 7794–7800.

[15] Prashant V. Kamat. “Quantum Dot Solar Cells. Semiconductor Nanocrystals as Light Harvesters”. In: *The Journal of Physical Chemistry C* 112.48 (Oct. 2008), pp. 18737–18753. DOI: `https://doi.org/10.1021/jp806791s`.

[16] Gao-Ling Yang and Hai-Zheng Zhong. “Organometal halide perovskite quantum dots: synthesis, optical properties, and display applications”. In: *Chinese Chemical Letters* 27.8 (Aug. 2016), pp. 1124–1130. DOI: `https://doi.org/10.1016/j.cclet.2016.06.047`.

[17] Dan Wang et al. “Polarized emission from CsPbX3 perovskite quantum dots”. In: *Nanoscale* 8.22 (2016), pp. 11565–11570. DOI: `10.1039/C6NR01915C`.

[18] Akihiro Kojima et al. “Organometal Halide Perovskites as Visible-Light Sensitizers for Photovoltaic Cells”. In: *Journal of the American Chemical Society* 131.17 (May 2009), pp. 6050–6051. DOI: `https://doi.org/10.1021/ja809598r`.

[19] M. Tuan Trinh et al. “Anomalous Independence of Multiple Exciton Generation on Different Group IV-VI Quantum Dot Architectures”. In: *Nano Letters* 11.4 (Apr. 2011), pp. 1623–1629. DOI: `https://doi.org/10.1021/nl200014g`.

[20] Michael G. Debije and Paul P. C. Verbunt. “Thirty Years of Luminescent Solar Concentrator Research: Solar Energy for the Built Environment”. In: *Advanced Energy Materials* 2.1 (Dec. 2011), pp. 12–35. DOI: `10.1002/aenm.201100554`.

[21] V. Sholin, J. D. Olson, and S. A. Carter. “Semiconducting polymers and quantum dots in luminescent solar concentrators for solar energy harvesting”. In: *Journal of Applied Physics* 101.12 (June 2007), p. 123114. DOI: `10.1063/1.2748350`.

[22] Michael G Debije and Paul PC Verbunt. “Thirty years of luminescent solar concentrator research: solar energy for the built environment”. In: *Advanced Energy Materials* 2.1 (2012), pp. 12–35.

[23] Concetta Nobile et al. “Self-assembly of highly fluorescent semiconductor nanorods into large scale smectic liquid crystal structures by coffee stain evaporation dynamics”. In: *Journal of Physics: Condensed Matter* 21.26 (2009), p. 264013.

[24] Wilfried GJHM Van Sark et al. “Luminescent Solar Concentrators-A review of recent results”. In: *Optics express* 16.26 (2008), pp. 21773–21792.

[25] JM Drake et al. “Organic dyes in PMMA in a planar luminescent solar collector: a performance evaluation”. In: *Applied Optics* 21.16 (1982), pp. 2945–2952.

[26] BA Swartz, T Cole, and AH Zewail. “Photon trapping and energy transfer in multiple-dye plastic matrices: an efficient solar-energy concentrator”. In: *Optics Letters* 1.2 (1977), pp. 73–75.

[27] Willes H Weber and John Lambe. “Luminescent greenhouse collector for solar radiation”. In: *Applied optics* 15.10 (1976), pp. 2299–2300.

[28] Renata Reisfeld, Dimitri Shamrakov, and Christian Jorgensen. “Photostable solar concentrators based on fluorescent glass films”. In: *Solar energy materials and solar cells* 33.4 (1994), pp. 417–427.

[29] JS Batchelder, AH Zewail, and T Cole. “Luminescent solar concentrators. 2: Experimental and theoretical analysis of their possible efficiencies”. In: *Applied Optics* 20.21 (1981), pp. 3733–3754.

[30] G Seybold and G Wagenblast. “New perylene and violanthrone dyestuffs for fluorescent collectors”. In: *Dyes and Pigments* 11.4 (1989), pp. 303–317.

[31] AJ Chatten et al. “Quantum dot solar concentrators”. In: *Semiconductors* 38.8 (2004), pp. 909–917.

[32] SJ Gallagher, B Norton, and PC Eames. “Quantum dot solar concentrators: electrical conversion efficiencies and comparative concentrating factors of fabricated devices”. In: *Solar Energy* 81.6 (2007), pp. 813–821.

[33] G. V. Shcherbatyuk et al. “Viability of using near infrared PbS quantum dots as active materials in luminescent solar concentrators”. In: *Applied Physics Letters* 96.19 (May 2010), p. 191901. DOI: `10.1063/1.3422485`.

[34] R Carmina Monreal, Tomasz J Antosiewicz, and S Peter Apell. “Competition between surface screening and size quantization for surface plasmons in nanoparticles”. In: *New Journal of Physics* 15.8 (Aug. 2013), p. 083044. DOI: `https://dx.doi.org/10.1088/1367-2630/15/8/083044`.

[35] Richard B M Schasfoort and Anna J Tudos, eds. *Handbook of Surface Plasmon Resonance*. Royal Society of Chemistry, 2008. DOI: `https://doi.org/10.1039/9781847558220`.

[36] William R. Erwin et al. “Light trapping in mesoporous solar cells with plasmonic nanostructures”. In: *Energy & Environmental Science* 9.5 (2016), pp. 1577–1601. DOI: `https://doi.org/10.1039/C5EE03847B`.

[37] Suljo Linic, Phillip Christopher, and David B. Ingram. “Plasmonic-metal nanostructures for efficient conversion of solar to chemical energy”. In: *Nature Materials* 10.12 (Nov. 2011), pp. 911–921. DOI: `https://doi.org/10.1038/nmat3151`.

[38] Xiaoguang Li, Di Xiao, and Zhenyu Zhang. “Landau damping of quantum plasmons in metal nanostructures”. In: *New Journal of Physics* 15.2 (Feb. 2013), p. 023011. DOI: `https://doi.org/10.1088/1367-2630/15/2/023011`.

[39] M. W. Knight et al. “Photodetection with Active Optical Antennas”. In: *Science* 332.6030 (May 2011), pp. 702–704. DOI: `10.1126/science.1203056`.

[40] Alejandro Manjavacas et al. “Plasmon-Induced Hot Carriers in Metallic Nanoparticles”. In: *ACS Nano* 8.8 (July 2014), pp. 7630–7638. DOI: `https://doi.org/10.1021/nn502445f`.

[41] Alexander O. Govorov, Hui Zhang, and Yurii K. Gun’ko. “Theory of Photoinjection of Hot Plasmonic Carriers from Metal Nanostructures into Semiconductors and Surface Molecules”. In: *The Journal of Physical Chemistry C* 117.32 (July 2013), pp. 16616–16631. DOI: `https://doi.org/10.1021/jp405430m`.

[42] Scott K. Cushing et al. “Controlling Plasmon-Induced Resonance Energy Transfer and Hot Electron Injection Processes in Metal@TiO2Core–Shell Nanoparticles”. In: *The Journal of Physical Chemistry C* 119.28 (June 2015), pp. 16239–16244. DOI: `https://doi.org/10.1021/acs.jpcc.5b03955`.

[43] Anatoliy Pinchuk and Uwe Kreibig. “Interface decay channel of particle surface plasmon resonance”. In: *New Journal of Physics* 5 (Nov. 2003), pp. 151–151. DOI: `https://doi.org/10.1088/1367-2630/5/1/151`.

[44] Ali Dabirian and Nima Taghavinia. “Theoretical study of light trapping in nanostructured thin film solar cells using wavelength-scale silver particles”. In: *ACS applied materials & interfaces* 7.27 (2015), pp. 14926–14932.

[45] Hua Dong et al. “Ag-encapsulated Au plasmonic nanorods for enhanced dye-sensitized solar cell performance”. In: *Journal of Materials Chemistry A* 3.8 (2015), pp. 4659–4668.

[46] Holly F Zarick et al. “Improving light harvesting in dye-sensitized solar cells using hybrid bimetallic nanostructures”. In: *ACS Photonics* 3.3 (2016), pp. 385–394.

[47] Gururaj V Naik et al. “Titanium nitride as a plasmonic material for visible and near-infrared wavelengths”. In: *Optical Materials Express* 2.4 (2012), pp. 478–489.

[48] Mark W Knight et al. “Aluminum for plasmonics”. In: *ACS nano* 8.1 (2014), pp. 834–840.

[49] Qi Xu et al. “Aluminum plasmonic nanoparticles enhanced dye sensitized solar cells”. In: *Optics express* 22.102 (2014), A301–A310.

[50] Sol Carretero-Palacios, Alberto Jiménez-Solano, and Hernán Mıguez. “Plasmonic nanoparticles as light-harvesting enhancers in perovskite solar cells: a user’s guide”. In: *ACS energy letters* 1.1 (2016), pp. 323–331.

[51] WEI Zhang et al. “Enhancement of perovskite-based solar cells employing core–shell metal nanoparticles”. In: *Nano letters* 13.9 (2013), pp. 4505–4510.

[52] Michael Saliba et al. “Plasmonic-Induced Photon Recycling in Metal Halide Perovskite Solar Cells”. In: *Advanced Functional Materials* 25.31 (2015), pp. 5038–5046.

[53] Evan T Vickers et al. “Improving charge carrier delocalization in perovskite quantum dots by surface passivation with conductive aromatic ligands”. In: *ACS Energy Letters* 3.12 (2018), pp. 2931–2939.

[54] Heinz-Helmut Perkampus. *UV-VIS Spectroscopy and its Applications*. Springer Science & Business Media, 2013.

[55] A. Goetzberger and W. Greube. “Solar energy conversion with fluorescent collectors”. In: *Applied Physics* 14.2 (Oct. 1977), pp. 123–139. DOI: `10.1007/bf00883080`.

[56] W. H. Weber and John Lambe. “Luminescent greenhouse collector for solar radiation”. In: *Applied Optics* 15.10 (Oct. 1976), p. 2299. DOI: `10.1364/ao.15.002299`.

[57] Michalis Kanellis et al. “The solar noise barrier project: 1. Effect of incident light orientation on the performance of a large-scale luminescent solar concentrator noise barrier”. In: *Renewable Energy* 103 (Apr. 2017), pp. 647–652. DOI: `10.1016/j.renene.2016.10.078`.

[58] Simon P. Philipps et al. *Current Status of Concentrator Photovoltaic (CPV) Technology*. Tech. rep. Dec. 2015. DOI: `10.2172/1351597`.

[59] Frank Dimroth et al. "Wafer bonded four-junction GaInP/GaAs//GaInAsP/GaInAs concentrator solar cells with 44.7% efficiency". In: *Progress in Photovoltaics: Research and Applications* 22.3 (Jan. 2014), pp. 277–282. DOI: `10.1002/pip.2475`.

[60] Igor Coropceanu and Moungi G. Bawendi. "Core/Shell Quantum Dot Based Luminescent Solar Concentrators with Reduced Reabsorption and Enhanced Efficiency". In: *Nano Letters* 14.7 (June 2014), pp. 4097–4101. DOI: `10.1021/nl501627e`.

[61] Meredith G. Hyldahl, Sheldon T. Bailey, and Bruce P. Wittmershaus. "Photostability and performance of CdSe/ZnS quantum dots in luminescent solar concentrators". In: *Solar Energy* 83.4 (Apr. 2009), pp. 566–573. DOI: `10.1016/j.solener.2008.10.001`.

[62] L. H. Slooff et al. "A luminescent solar concentrator with 7.1% power conversion efficiency". In: *physica status solidi (RRL) - Rapid Research Letters* 2.6 (Dec. 2008), pp. 257–259. DOI: `10.1002/pssr.200802186`.

[63] Mengxia Liu et al. "Hybrid organic–inorganic inks flatten the energy landscape in colloidal quantum dot solids". In: *Nature Materials* 16.2 (Nov. 2016), pp. 258–263. DOI: `10.1038/nmat4800`.

[64] Francesco Meinardi et al. "Large-area luminescent solar concentrators based on 'Stokes-shift-engineered' nanocrystals in a mass-polymerized PMMA matrix". In: *Nature Photonics* 8.5 (Apr. 2014), pp. 392–399. DOI: `10.1038/nphoton.2014.54`.

[65] Lorcan J. Brennan et al. "Large area quantum dot luminescent solar concentrators for use with dye-sensitised solar cells". In: *Journal of Materials Chemistry A* 6.6 (2018), pp. 2671–2680. DOI: `10.1039/c7ta04731b`.

[66] Yimu Zhao and Richard R. Lunt. "Transparent Luminescent Solar Concentrators for Large-Area Solar Windows Enabled by Massive Stokes-Shift Nanocluster Phosphors". In: *Advanced Energy Materials* 3.9 (Apr. 2013), pp. 1143–1148. DOI: `10.1002/aenm.201300173`.

[67] W. Nie et al. "High-efficiency solution-processed perovskite solar cells with millimeter-scale grains". In: *Science* 347.6221 (Jan. 2015), pp. 522–525. DOI: `10.1126/science.aaa0472`.

[68] Martin A. Green et al. "Solar cell efficiency tables (version 52)". In: *Progress in Photovoltaics: Research and Applications* 26.7 (June 2018), pp. 427–436. DOI: `10.1002/pip.3040`.

[69] Taame Abraha Berhe et al. "Organometal halide perovskite solar cells: degradation and stability". In: *Energy & Environmental Science* 9.2 (2016), pp. 323–356. DOI: `10.1039/c5ee02733k`.

[70] Jeffrey A. Christians et al. "Tailored interfaces of unencapsulated perovskite solar cells for 1,000 hour operational stability". In: *Nature Energy* 3.1 (Jan. 2018), pp. 68–74. DOI: `10.1038/s41560-017-0067-y`.

[71] Jacky Even, Laurent Pedesseau, and Claudine Katan. "Analysis of Multivalley and Multibandgap Absorption and Enhancement of Free Carriers Related to Exciton Screening in Hybrid Perovskites". In: *The Journal of Physical Chemistry C* 118.22 (May 2014), pp. 11566–11572. DOI: `10.1021/jp503337a`.

[72] Katerina Nikolaidou et al. "Hybrid Perovskite Thin Films as Highly Efficient Luminescent Solar Concentrators". In: *Advanced Optical Materials* 4.12 (Sept. 2016), pp. 2126–2132. DOI: `10.1002/adom.201600634`.

[73] M.B. de la Mora et al. "Materials for downconversion in solar cells: Perspectives and challenges". In: *Solar Energy Materials and Solar Cells* 165 (June 2017), pp. 59–71. DOI: `10.1016/j.solmat.2017.02.016`.

[74] Teddy Salim et al. "Perovskite-based solar cells: impact of morphology and device architecture on device performance". In: *Journal of Materials Chemistry A* 3.17 (2015), pp. 8943–8969. DOI: `10.1039/c4ta05226a`.

[75] Hidetaka Ishihara et al. "Electrohydrodynamically Assisted Deposition of Efficient Perovskite Photovoltaics". In: *Advanced Materials Interfaces* 3.9 (Feb. 2016), p. 1500762. DOI: `10.1002/admi.201500762`.

[76] Alexander Sharenko and Michael F. Toney. "Relationships between Lead Halide Perovskite Thin-Film Fabrication, Morphology, and Performance in Solar Cells". In: *Journal of the American Chemical Society* 138.2 (Nov. 2015), pp. 463–470. DOI: `10.1021/jacs.5b10723`.

[77] Wei Zhang et al. "Ultrasmooth organic–inorganic perovskite thin-film formation and crystallization for efficient planar heterojunction solar cells". In: *Nature Communications* 6.1 (Jan. 2015). DOI: `10.1038/ncomms7142`.

[78] Wan-Jian Yin, Tingting Shi, and Yanfa Yan. "Unique Properties of Halide Perovskites as Possible Origins of the Superior Solar Cell Performance". In: *Advanced Materials* 26.27 (May 2014), pp. 4653–4658. DOI: `10.1002/adma.201306281`.

[79] D. W. de Quilettes et al. "Impact of microstructure on local carrier lifetime in perovskite solar cells". In: *Science* 348.6235 (Apr. 2015), pp. 683–686. DOI: `10.1126/science.aaa5333`.

[80] Derya Sahin and Boaz Ilan. “Radiative transport theory for light propagation in luminescent media”. In: *Journal of the Optical Society of America A* 30.5 (Apr. 2013), p. 813. DOI: `10.1364/josaa.30.000813`.

[81] Arthur J Nozik et al. “Semiconductor quantum dots and quantum dot arrays and applications of multiple exciton generation to third-generation photovoltaic solar cells”. In: *Chemical reviews* 110.11 (2010), pp. 6873–6890.

[82] Atature Kiraz, M Atatüre, and A Imamoğlu. “Quantum-dot single-photon sources: Prospects for applications in linear optics quantum-information processing”. In: *Physical Review A* 69.3 (2004), p. 032305.

[83] Igor L Medintz and Hedi Mattoussi. “Quantum dot-based resonance energy transfer and its growing application in biology”. In: *Physical Chemistry Chemical Physics* 11.1 (2009), pp. 17–45.

[84] Yue Wang et al. “All-inorganic colloidal perovskite quantum dots: a new class of lasing materials with favorable characteristics”. In: *Advanced materials* 27.44 (2015), pp. 7101–7108.

[85] Hung-Chia Wang et al. “Perovskite quantum dots and their application in light-emitting diodes”. In: *Small* 14.1 (2018), p. 1702433.

[86] Nils Calander and Magnus Willander. “Theory of surface-plasmon resonance optical-field enhancement at prolate spheroids”. In: *Journal of applied physics* 92.9 (2002), pp. 4878–4884.

[87] DaeGwi Kim et al. “Precise control of photoluminescence enhancement and quenching of semiconductor quantum dots using localized surface plasmons in metal nanoparticles”. In: *Journal of Applied Physics* 114.15 (2013), p. 154307.

[88] M Haridas, LN Tripathi, and JK Basu. “Photoluminescence enhancement and quenching in metal-semiconductor quantum dot hybrid arrays”. In: *Applied Physics Letters* 98.6 (2011), p. 27.

[89] Gang Logan Liu et al. “Quantized plasmon quenching dips nanospectroscopy via plasmon resonance energy transfer”. In: *Nature Methods* 4.12 (2007), pp. 1015–1017.

[90] Jamuna K Vaishnav and Tushar Kanti Mukherjee. “Long-range resonance coupling-induced surface energy transfer from CdTe quantum dot to plasmonic nanoparticle”. In: *The Journal of Physical Chemistry C* 122.49 (2018), pp. 28324–28336.

[91] Shengye Jin et al. “Distance-engineered plasmon-enhanced light harvesting in CdSe quantum dots”. In: *The Journal of Physical Chemistry Letters* 4.20 (2013), pp. 3527–3533.

[92] WL Barnes. “Fluorescence near interfaces: the role of photonic mode density”. In: *journal of modern optics* 45.4 (1998), pp. 661–699.

[93] Subhash Chandra et al. “Enhanced quantum dot emission for luminescent solar concentrators using plasmonic interaction”. In: *Solar energy materials and solar cells* 98 (2012), pp. 385–390.

[94] Pascal Anger, Palash Bharadwaj, and Lukas Novotny. “Enhancement and quenching of single-molecule fluorescence”. In: *Physical review letters* 96.11 (2006), p. 113002.

[95] O Stranik et al. “Plasmonic enhancement of fluorescence for sensor applications”. In: *Sensors and Actuators B: Chemical* 107.1 (2005), pp. 148–153.

[96] Yeechi Chen et al. “Excitation enhancement of CdSe quantum dots by single metal nanoparticles”. In: *Applied Physics Letters* 93.5 (2008), p. 053106.

[97] Yeechi Chen, Keiko Munechika, and David S Ginger. “Dependence of fluorescence intensity on the spectral overlap between fluorophores and plasmon resonant single silver nanoparticles”. In: *Nano letters* 7.3 (2007), pp. 690–696.

[98] Julie S Biteen et al. “Enhanced radiative emission rate and quantum efficiency in coupled silicon nanocrystal-nanostructured gold emitters”. In: *Nano letters* 5.9 (2005), pp. 1768–1773.

[99] Jörg P Kottmann et al. “Dramatic localized electromagnetic enhancement in plasmon resonant nanowires”. In: *Chemical Physics Letters* 341.1-2 (2001), pp. 1–6.

[100] D Kovalev et al. “Optical absorption cross sections of Si nanocrystals”. In: *Physical Review B* 61.7 (2000), p. 4485.

[101] Jiangtian Li et al. “Plasmon-induced resonance energy transfer for solar energy conversion”. In: *Nature Photonics* 9.9 (2015), pp. 601–607.

[102] Dapeng Wu et al. “Plasmon resonance energy transfer and hot electron injection induced high photocurrent density in liquid junction Ag@ Ag 2 S sensitized solar cells”. In: *Dalton Transactions* 45.41 (2016), pp. 16275–16282.

[103] Yuhua Lu et al. “Gap-plasmon based broadband absorbers for enhanced hot-electron and photocurrent generation”. In: *Scientific reports* 6.1 (2016), pp. 1–9.

[104] Andrea E Schlather et al. “Near-field mediated plexcitonic coupling and giant Rabi splitting in individual metallic dimers”. In: *Nano letters* 13.7 (2013), pp. 3281–3286.

[105] Z Liu et al. *Fano resonance Rabi splitting of surface plasmons Sci*. 2017.

[106] Mykhaylo M Dvoynenko. “About possibility of strong coupling between single molecule and surface plasmons”. In: *arXiv preprint arXiv:1202.2535* (2012).

[107] Haiguang Zhao et al. “Perovskite quantum dots integrated in large-area luminescent solar concentrators”. In: *Nano Energy* 37 (2017), pp. 214–223.

[108] Haiguang Zhao et al. “Efficient and stable tandem luminescent solar concentrators based on carbon dots and perovskite quantum dots”. In: *Nano Energy* 50 (2018), pp. 756–765.

[109] Qingyang Lu et al. “Improving power conversion efficiency in luminescent solar concentrators using nanoparticle fluorescence and scattering”. In: *Nanotechnology* 31.45 (2020), p. 455205.

[110] Haiguang Zhao et al. “Absorption Enhancement in “Giant” Core/Alloyed-Shell Quantum Dots for Luminescent Solar Concentrator”. In: *Small* 12.38 (2016), pp. 5354–5365.

[111] Yufeng Zhou et al. “Near infrared, highly efficient luminescent solar concentrators”. In: *Advanced Energy Materials* 6.11 (2016), p. 1501913.

[112] Francesco Meinardi et al. “Highly efficient luminescent solar concentrators based on earth-abundant indirect-bandgap silicon quantum dots”. In: *Nature Photonics* 11.3 (2017), pp. 177–185.

[113] Francesco Meinardi et al. “Highly efficient large-area colourless luminescent solar concentrators using heavy-metal-free colloidal quantum dots”. In: *Nature nanotechnology* 10.10 (2015), pp. 878–885.